



TECHNISCHE  
UNIVERSITÄT  
WIEN  
Vienna | Austria

MASTER THESIS

# Synthesis and characterization of $\text{Co}_x(\text{SR})_m$ and $\text{Co}_x\text{Au}_{25-x}(\text{SR})_m$ cluster catalysts

carried out at the  
Institute of Materials Chemistry  
of TU Wien

under the supervision of  
Univ.Prof. Dr. Günther Rupprechter  
Dr. Noelia Barrabés

by  
Stephan Pollitt, BSc.

Ullmannstraße 14/6  
A-1150 Vienna

Vienna, 7.12.2017



TECHNISCHE  
UNIVERSITÄT  
WIEN  
Vienna | Austria

DIPLOMARBEIT

# Synthese und Charakterisierung von $\text{Co}_x(\text{SR})_m$ und $\text{Co}_x\text{Au}_{25-x}(\text{SR})_m$ Cluster Katalysatoren

ausgeführt am Institut für  
Materialchemie  
der Technischen Universität Wien

unter der Anleitung von  
Univ.Prof. Dr. Günther Rupprechter  
Dr. Noelia Barrabés

durch  
Stephan Pollitt, BSc.

Ullmannstraße 14/6  
A-1150 Wien

Wien, 7.12.2017

STATUTORY DECLARATION: I hereby declare that I have authored this thesis independently, that I have not used other than the declared sources/resources, and that I have explicitly marked all material which has been quoted either literally or by content from the used sources.

EIDESSTATTLICHE ERKLÄRUNG: Ich erkläre hiermit an Eides statt, dass ich die vorliegende Arbeit selbstständig verfasst, andere als die angegebenen Quellen/Hilfsmittel nicht benutzt, und die den benutzten Quellen wörtlich und inhaltlich entnommenen Stellen als solche kenntlich gemacht habe.

# Abstract

Thiolate protected nanoclusters with less than 100 atoms have recently become an intensively studied field, due to their outstanding properties resulting from non-bulk like structures and electronic configurations. The controlled design at atomic scale, controlling the number of atoms, but also metal composition or ligand functionalization, enables a broad field of applications.

Monodisperse clusters with resolved structures constitute well-suited optimal active phases for catalytic studies. Therefore, the present Master Thesis is focused on the design and synthesis of novel thiolate protected Co- and Co/Au-nanoclusters, as well as on the characterization of their properties, especially catalytic application.

$\text{Co}_x(\text{SR})_m$  clusters in the size range of 2 nm were successfully synthesized for the first time, expanding the variety of thiolate protected metal clusters. These clusters have specific structure elements like a core in metallic state, which was determined by XPS, XAFS and EELS, and characteristic staple motifs, which were revealed by MALDI and Raman. Furthermore, cobalt doped thiolate protected gold nanoclusters were synthesized by two different approaches. Preliminary information on cluster composition ( $\text{CoAu}_{24}(\text{SR})_{18}$ ) was obtained by MALDI. The number of dopant atoms and their exact location is debated and may vary between the cluster core and staples, as based on the S K-edge XAFS, UV/Vis spectroscopy and DFT calculations.

The synthesized clusters were supported on  $\text{CeO}_2$  by impregnation and the exact composition was determined by GIXRF. The stability and catalytic activity were tested in CO oxidation as model reaction. The prepared catalysts were pretreated and the removal of ligands was followed by XAFS. Supported  $\text{Co}_x(\text{SR})_m$  did not show any activity. For the Co/Au catalyst, in-situ DRIFTS-MS revealed a strong impact of cobalt doping on the reaction behavior, lowering the reaction onset temperature by 50 °C, as compared to a pure  $\text{Au}_{25}\text{-CeO}_2$  catalyst.

# Abstract

Diese Masterarbeit hatte die erstmalige Synthese und Charakterisierung von ligandenstabilisierte Co- und Co/Au-Nanocluster zum Ziel, da monodisperse Cluster mit bekannter Struktur ideale Materialien für die Katalysatorforschung sind.

Thiol-ligandenstabilisierte Nanocluster, die aus weniger als 100 Atome bestehen, wurden letztthin aufgrund ihrer speziellen Eigenschaften intensiv untersucht. Ihre Besonderheiten sind auf ihre Strukturen und Elektronenkonfigurationen zurückzuführen, welche sich deutlich von denen größerer „bulk“ Partikel unterscheiden. Die Möglichkeit zur gezielten Kontrolle - auf atomarer Ebene - der Atomanzahl, der Metallzusammensetzung (Dotierung) und Funktionalisierung der Liganden eröffnet eine Vielzahl an Anwendungsgebieten.

$\text{Co}_x(\text{SR})_m$  Cluster mit einer Größe von 2 nm konnten zum ersten Mal erfolgreich synthetisiert werden und erweitern damit das Spektrum an thiol-ligandenstabilisierten metallischen Nanoclustern. Diese Cluster haben charakteristische Strukturelemente. Der Kern ist metallisch, was durch XPS, XAFS und EELS festgestellt wurde. Ebenso müssen „Staple-Bindungen“ vorhanden sein, was durch Raman und MALDI verifiziert wurde.

Zusätzlich wurden kobaltdotierte Goldnanocluster auf zwei Wege synthetisiert. Eine vorläufige Zusammensetzung ( $\text{CoAu}_{24}(\text{SR})_{18}$ ) wurde mittels MALDI ermittelt. Die Position der Co-Dotierung konnte mittels S K-edge XAFS und UV/Vis, unterstützt durch DFT-Berechnungen, festgestellt werden: in der Oberfläche des Au-Clusterkerns oder in den Staple-Bindungen.

Die synthetisierten Cluster wurden auf  $\text{CeO}_2$  deponiert und mittels GIXRF quantifiziert. Aktivitäts- und Stabilitätsstudien wurden für die Kohlenmonoxid-Oxidation als Modellreaktion durchgeführt. Die Katalysatoren wurden vorbehandelt, wobei das Brechen der Staple-Bindungen mittels XAFS beobachtet wurde.  $\text{Co}_x(\text{SR})_m\text{-CeO}_2$  zeigte keine CO-Umsatz, allerdings wurde ein starker Einfluss der Kobaltdotierung auf das Reaktionsverhalten festgestellt. Im Vergleich zu einem reinen  $\text{Au}_{25}$ -Katalysator wurde die anfängliche Reaktionstemperatur um  $50^\circ\text{C}$  gesenkt.

# Contents

<b>I</b>	<b>Introduction</b>	<b>1</b>
<b>II</b>	<b>Motivation</b>	<b>6</b>
<b>III</b>	<b>Experimental</b>	<b>7</b>
III-1	Synthesis . . . . .	7
1	$\text{Co}_x(\text{SR})_m$ clusters . . . . .	7
2	$\text{Co}_x\text{Au}_{25-x}(\text{SR})_y$ Synthesis 1 (S1) . . . . .	8
3	$\text{Co}_x\text{Au}_{25-x}(\text{SR})_y$ Synthesis 2 (S2) . . . . .	8
4	$\text{Au}_{25}(\text{SR})_{18}$ . . . . .	9
III-2	Size exclusion chromatography (SEC) . . . . .	10
III-3	Catalyst preparation . . . . .	10
III-4	Characterization techniques . . . . .	11
1	UV/Vis spectroscopy . . . . .	11
2	MALDI . . . . .	11
3	Electron microscopy . . . . .	11
4	Raman spectroscopy . . . . .	12
5	X-ray photoelectron spectroscopy (XPS) . . . . .	12
6	Scanning Tunneling Microscopy (STM) . . . . .	12
7	Grazing incidence X-ray fluorescence analysis (GIXRF) . . . . .	13
III-5	X-ray absorption fine structure spectroscopy (XAFS) . . . . .	13
III-6	In-situ DRIFTS measurements . . . . .	14
III-7	Catalytic activity tests . . . . .	15
1	Cell preparation . . . . .	16
<b>IV</b>	<b><math>\text{Co}_x(\text{SR})_m</math> cluster</b>	<b>17</b>
IV-1	Synthesis of $\text{Co}_x(\text{SR})_m$ clusters . . . . .	17
IV-2	Characterisation of $\text{Co}_x(\text{SR})_m$ . . . . .	18
1	MALDI-TOF-MS . . . . .	18
2	TGA . . . . .	20
3	XRD . . . . .	21

4	UV/Vis and Photoluminescence Spectroscopy . . . . .	22
5	Electron Microscopy . . . . .	25
6	STM . . . . .	27
7	Vibrational Spectroscopy . . . . .	29
8	XPS . . . . .	31
9	XAFS . . . . .	32
IV-3	Conclusions $\text{Co}_x(\text{SR})_m$ . . . . .	33
<b>V</b>	<b><math>\text{Co}_x\text{Au}_{25-x}(\text{SR})_y</math> cluster</b>	<b>34</b>
V-1	$\text{Co}_x\text{Au}_{25-x}(\text{SR})_y$ S1 . . . . .	34
1	Characterisation of $\text{Co}_x\text{Au}_{25-x}(\text{SR})_y$ S1 . . . . .	34
V-2	$\text{Co}_x\text{Au}_{25-x}(\text{SR})_y$ S2 . . . . .	36
1	Characterization of $\text{Co}_x\text{Au}_{25-x}(\text{SR})_y$ S2 . . . . .	37
2	Theoretical calculations on $\text{Co}_x\text{Au}_{25-x}(\text{SR})_y$ clusters S2 . . . . .	39
V-3	Conclusions of $\text{Co}_x\text{Au}_{25-x}(\text{SR})_y$ . . . . .	41
<b>VI</b>	<b>Catalytic Properties</b>	<b>42</b>
VI-1	Catalyst characterization . . . . .	42
VI-2	Catalytic activity in CO oxidation . . . . .	44
VI-3	In situ DRIFT studies . . . . .	46
VI-4	XAFS . . . . .	47
VI-5	Conclusions of Catalytic Properties . . . . .	49
<b>VII</b>	<b>Discussion</b>	<b>50</b>
<b>VIII</b>	<b>Appendix</b>	<b>52</b>
1	Supporting information . . . . .	52
2	References . . . . .	54

# List of Figures

I.1	Structures of gold particles from nanoscale to bulk. The graphic was reproduced from Negishi et al. <sup>[10]</sup> . . . . .	1
I.2	Relation of particle size, structure and electronic structure of particles. The graphic was reproduced from Yamazoe et al. <sup>[11]</sup> . . . . .	2
I.3	Structure of Au <sub>25</sub> (SR) <sub>18</sub> . Upper left: core; center: core with staple motifs; bottom right: complete structure. Adapted from Kulesza <sup>[14]</sup> . . . . .	3
III.1	Size exclusion chromatography (SEC) . . . . .	10
III.2	XAFS in-situ reaction setup (SLS) . . . . .	14
III.3	DRIFTS in-situ reaction setup (PSI) . . . . .	15
III.4	Left: Reactor cell filled with catalyst. Right: Exploded view of reactor cell. Adapted from Chiarello et al. <sup>[52]</sup> . . . . .	15
IV.1	MALDI-TOF-MS spectrum of the prepared Co <sub>x</sub> (SR) <sub>m</sub> clusters. . . . .	19
IV.2	Staple motif of Co-clusters. Co (magenta), S (green) . . . . .	20
IV.3	Thermogravimetric analysis of Co <sub>x</sub> (SC <sub>2</sub> H <sub>4</sub> Ph) <sub>m</sub> clusters. . . . .	21
IV.4	Comparison between Co-clusters and bulk Co with X-ray powder diffraction. . . . .	22
IV.5	UV/Vis spectrum of Co clusters in dichloromethane. . . . .	23
IV.6	Comparison of UV/Vis spectra of Co nanoparticles (with SC <sub>2</sub> H <sub>4</sub> Ph ligands) and Co <sub>x</sub> (SC <sub>2</sub> H <sub>4</sub> Ph) <sub>m</sub> clusters dissolved in dichloromethane. . . . .	24
IV.7	Photoluminescence spectrum of Co clusters. Co clusters in dichloromethane solution are shown as inset, with UV/Vis illumination ( $\lambda$ from 220 nm to 400 nm). . . . .	25
IV.8	STEM image of Co <sub>x</sub> (SR) <sub>18</sub> . . . . .	26
IV.9	EDX spectrum of Co nanoparticles . . . . .	26
IV.10	HAADF with EELS mapping region. Co L-edge signal map (blue), C K-edge (red), S L-edge (yellow) . . . . .	26
IV.11	EELS Co L <sub>3</sub> spectrum showing metallic Co . . . . .	27
IV.12	SAED . . . . .	27



IV.13	STM image of Co clusters supported on HOPG, taken at room temperature ( $V_{\text{sample}}=1.6\text{ V}$ , $I_{\text{tunnel}}=0.35\text{ nA}$ ). The cluster size is around 1.3 nm. . . . .	28
IV.14	STM topography and corresponding line profiles of cobalt clusters on HOPG. . . . .	28
IV.15	Raman spectra of $\text{Co}_x(\text{SR})_m$ . . . . .	29
IV.16	Left: MIR; Right: FIR FTIR spectra of $\text{Co}_x(\text{SR})_m$ clusters. . . . .	30
IV.17	(a) XPS spectra of the Co $2p_{3/2}$ ; (b) the S $2p_{3/2}$ and S $2p_{1/2}$ core level shifts of the $\text{Co}_x(\text{SR})_m$ clusters on HOPG. . . . .	32
IV.18	(a) XANES spectra at the Co K-edge and (b) S K-edge of the $\text{Co}_x(\text{SR})_m$ clusters and reference materials. . . . .	33
V.1	UV/Vis spectra of fractions from SEC of synthesis S1 . . . . .	35
V.2	UV/Vis spectrum of $\text{Au}_{25}(\text{SR})_{18}$ . . . . .	35
V.3	MALDI spectra of the fractions 6, 8, 9, 10, 11 and 12. . . . .	36
V.4	UV/Vis spectra after SEC of the purest fraction from solvent extraction. . . . .	37
V.5	MALDI spectra of acetonitril, acetone and DCM fraction. . . . .	38
V.6	XAFS of doped gold clusters and references: Left: S K-edge, XANES Right: Au $L_3$ -edge, R-space . . . . .	39
V.7	Calculated UV/Vis spectra of $\text{CoAu}_{24}(\text{SR})_{18}$ nanoclusters with different dopant positions . . . . .	40
V.8	Comparison of experimental and calculated data . . . . .	40
VI.1	GIXRF spectrum and fitting of the Au/Co-CeO <sub>2</sub> catalyst . . . . .	43
VI.2	GIXRF spectrum and fitting of the $\text{Au}_{25}$ -CeO <sub>2</sub> catalyst . . . . .	43
VI.3	MS spectra of CO, CO <sub>2</sub> , H <sub>2</sub> O and O <sub>2</sub> during CO-oxidation on Au/Co-CeO <sub>2</sub> catalyst. . . . .	44
VI.4	Hysteresis of CO conversion on Au/Co-CeO <sub>2</sub> catalyst. . . . .	44
VI.5	MS spectra of CO, CO <sub>2</sub> , H <sub>2</sub> O and O <sub>2</sub> during CO-oxidation experiment on $\text{Au}_{25}$ -CeO <sub>2</sub> catalyst. . . . .	45
VI.6	Hysteresis of CO conversion on $\text{Au}_{25}$ -CeO <sub>2</sub> catalyst. . . . .	45
VI.7	Comparison of the CO oxidation activity: normalized CO <sub>2</sub> MS signal of Au/Co-CeO <sub>2</sub> and $\text{Au}_{25}$ -CeO <sub>2</sub> catalyst. . . . .	46
VI.8	DRIFT spectra of CoAu catalyst under reaction conditions at different temperatures. . . . .	47
VI.9	XAFS $L_3$ : XANES region of Au/Co catalyst on CeO <sub>2</sub> : fresh, after pretreatment and after reaction . . . . .	48
VI.10	XAFS Au $L_3$ : R-space of Au/Co on CeO <sub>2</sub> catalyst: fresh, after pretreatment and after reaction. . . . .	49

VIII.1 Temperature dependency of the half life time of AIBN (red). The graphic was reproduced from Wako <sup>[95]</sup> . . . . .	52
VIII.2 Calculations of XANES spectra of Au <sub>38</sub> (SR) <sub>24</sub> L <sub>3</sub> -edge with FEFF9 <sup>[100]</sup> . . . . .	53

# List of Tables

III.1 Reagents of $\text{Co}_x(\text{SR})_m$ Synthesis . . . . .	7
III.2 Reagents of Synthesis S1 . . . . .	8
III.3 Reagents of Synthesis S2 . . . . .	9
III.4 Reagents of $\text{Au}_{25}(\text{SR})_{18}$ Synthesis . . . . .	9
III.5 Reagents of $\text{CeO}_2$ combustion synthesis . . . . .	10
VI.1 Weight and atomic ratio of Ce, Au and Co from Au/Co- $\text{CeO}_2$ and $\text{Au}_{25}$ - $\text{CeO}_2$ catalysts. . . . .	43

# Chapter I

## Introduction

Metal nanoclusters with less than 100 atoms have recently become an intensively studied field, due to their size-dependent properties, which do not follow the common scaling laws of bulk materials. The difference between typically polydisperse nanoparticles and monodisperse nanoclusters is the knowledge of the exact atom number and composition of the clusters. As shown in Figure I.1, by decreasing the number of atoms, different structures differing from fcc gold can be obtained; for example icosahedra, which fivefold rotation axis are quite uncommon in bulk materials. Furthermore, by decreasing the particle size, the relation of surface atoms to core atoms changes drastically, which leads to an excess of energy that can be used for applications like catalysis. As shown in Figure I.2, due to unique structures and low atom numbers ( $<100$ ), quantum size effects lead to different electronic states, redox-, photoluminescent-, magnetic and catalytic properties<sup>[1,2,3,4]</sup>. This opens to a variety of potential applications in sensor technology<sup>[5,6]</sup>, biomedicine<sup>[7]</sup>, nanoelectronics and catalysis<sup>[1,8,9]</sup>.

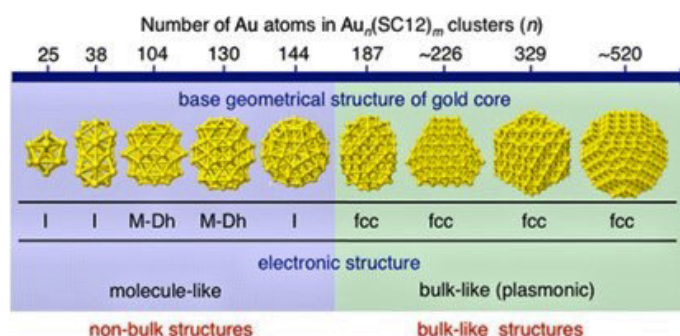


Figure I.1: Structures of gold particles from nanoscale to bulk. The graphic was reproduced from Negishi et al.<sup>[10]</sup>.

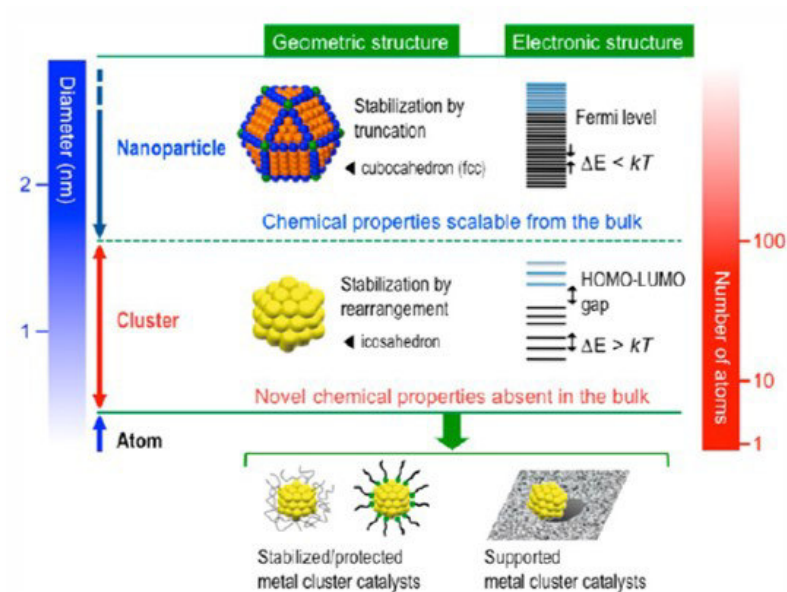


Figure I.2: Relation of particle size, structure and electronic structure of particles. The graphic was reproduced from Yamazoe et al.<sup>[11]</sup>.

Thiolate protected gold clusters exhibit a high stability due to their characteristic structure elements; Figure I.3 shows the dissected  $\text{Au}_{25}(\text{SR})_{18}$  cluster structure. The model of a core in a cage from Iwasa and Nobusada<sup>[12]</sup> was calculated by DFT and later proven by single crystal XRD by Zhu et al.<sup>[13]</sup>. The core of the cluster is in metallic state and surrounded by "staple motifs". Those are alternating Au and S atoms ( $-\text{S}(\text{R})-\text{Au}-\text{S}(\text{R})-\text{Au}-\text{S}(\text{R})-$ ) with covalent bonds, which stabilize the cluster structure. Each sulfur is bonded to an organic group which is responsible for properties like solubility, chirality etc.

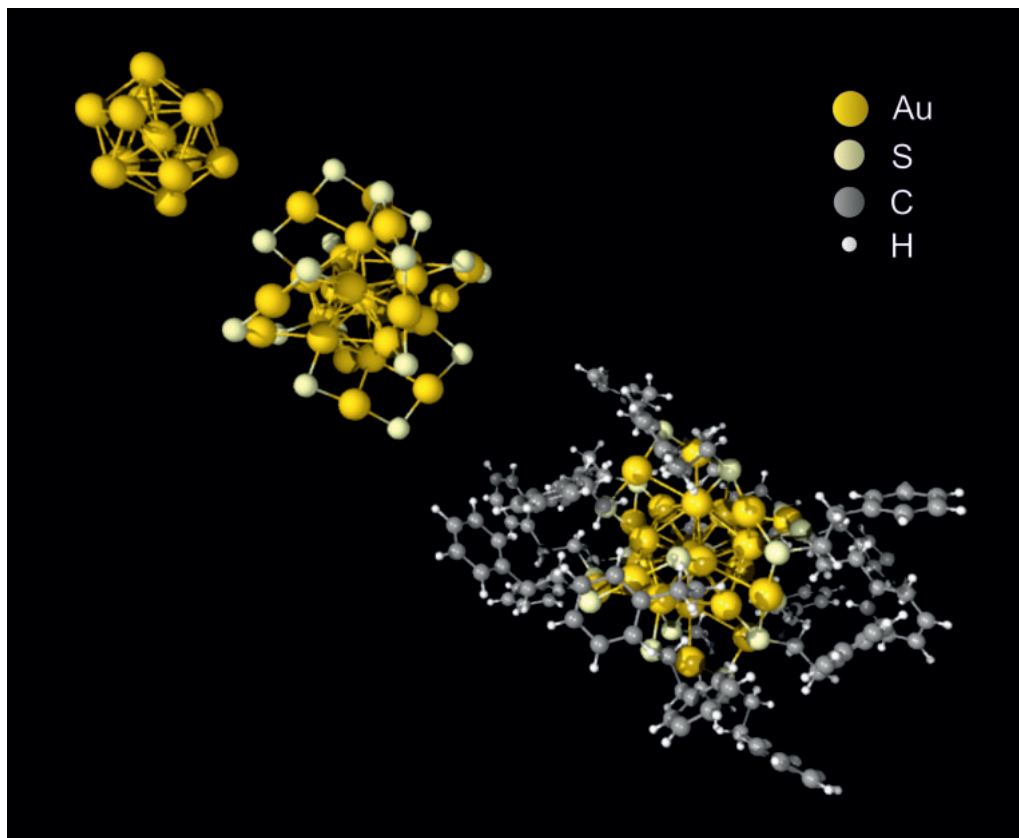


Figure I.3: Structure of  $\text{Au}_{25}(\text{SR})_{18}$ . Upper left: core; center: core with staple motifs; bottom right: complete structure. Adapted from Kulesza<sup>[14]</sup>.

Previous research activities during the last decade have focused on thiolate protected Au and Ag clusters, including optimization of different atomic sizes, composition (bi-, tri-metallic clusters) and structure, revealing exciting properties at the nanoscale<sup>[1]</sup>. However, metal nanoclusters other than gold or silver have rarely been studied, due to difficulties in successfully synthesizing stable structures in the range of a few atoms. Recently, new metal clusters such as  $\text{Ni}_x(\text{SC}_2\text{H}_4\text{Ph})_m$  ( $x=6,39,41$ )<sup>[15,16,17]</sup>,  $\text{Cu}_{38}(\text{SC}_2\text{H}_4\text{Ph})_{25}$ <sup>[18]</sup>, or  $\text{Ir}_9(\text{SC}_2\text{H}_4\text{Ph})_6$ <sup>[19]</sup> have been reported, showing enhanced properties when compared with pure metal nanoparticles.

**Cobalt (Co)** is a metal with low ionization potential for d-electrons and exhibits size-dependent structural, magnetic, electronic and catalytic properties. The exponential dependence of the magnetization relaxation time on volume has stimulated intensive studies of Co nanocrystal synthesis for magnetic storage applications<sup>[20]</sup>. However, unlike gold or silver, zero-valent cobalt nanometal is very sensitive to oxidation, creating a challenge to stabilize cobalt nanoparticles in different media. A few preceding studies have shown that via passivation by organic thiols the oxidation and agglomeration of metallic Co particles can be avoided,

which would lead to particles in the micron size<sup>[21,22]</sup>.

In addition, several recent studies have focused on the synthesis of defined cobalt sulfide (CoS<sub>2</sub>) nanostructures. Cobalt sulfides have phase-dependent electronic, magnetic and catalytic properties, opening potential applications in energy conversion and storage. Due the low overpotential, high durability and good cyclability, CoS<sub>2</sub> may also be used in batteries. CoS<sub>2</sub> also showed high capacitance in electrochemical capacitors due to its high redox activity, for example in dye-sensitized solar cells. High efficiency of CoS<sub>2</sub> has been also observed in hydrogen evolution electrocatalysis<sup>[23,24]</sup> and photoelectrochemical<sup>[25]</sup> processes<sup>[26,27,28]</sup>. Thus, thiolated cobalt nanoclusters may represent an interesting approach towards well defined cobalt sulfide nanostructures, with great potential in several applications.

As mentioned, cobalt exhibits loosely bonded d-electrons and high electrical conductivity, which makes it suitable for catalytic applications both in metallic and oxidic form. Obtaining truly homogeneous and well-defined nanostructures is very beneficial for understanding catalytic reaction mechanisms on an atomic level, since it typically depends on nanoparticle size and structure. For example, when cobalt oxides were grown from colloidal cobalt particles of defined size, better insights into their CO oxidation activity were obtained<sup>[29]</sup>. Colloidal particles are usually polydisperse, so that monodisperse cobalt nanoclusters with defined structure could be a better precursor for growing structurally well-defined cobalt oxides. Consequently, the successful synthesis of cobalt nanostructures would be very rewarding, enabling a broad range of applications in catalytic, photo-, and electrochemical processes.

Recently **bimetallic thiolate protected nanoclusters** have received attention due to catalytic research. Doping by metal atoms like Hg, Cd, Pd, Pt and Cu into well known gold nanoclusters enables fine tuning of cluster properties and can increase their stability. Changes in atomic composition and coordination leads to different electronic configuration, which then affect the properties. Dopant atoms can be located in different positions of the cluster structure, such as the center, core or staples. Yao et al. compared Hg and Cd dopants in Au<sub>25</sub>(SR)<sub>18</sub> clusters and found Cd located in the core, whereas Hg was occupying the staples<sup>[30]</sup>. Christensen et al. found Pt and Negishi et al. found Pd only to take the center position of a Au<sub>25</sub>(SR)<sub>18</sub> cluster core<sup>[31,32]</sup>. Doped thiolate protected nanoclusters can be synthesized either directly from two metal salts or by offering metal ions to a cluster solution<sup>[32,33,34,35]</sup>. Previous work has shown<sup>[32]</sup> that atomically precise bimetallic clusters have an enhancement effect in several reactions compared

to un-doped clusters<sup>[36,37,38]</sup> that can be related to changes in the electronic configuration depending on the dopant position. Negishi et al. demonstrated a change in electronic structure and redox potential once a gold cluster was doped with copper<sup>[35]</sup> and Qian et al. proved an enhancement effect of monoplatinum doped  $\text{Au}_{25}(\text{SR})_{18}$  clusters in styrene oxidation<sup>[39]</sup>. Thiolate protected clusters thus offer the possibility to create new atomically designed bimetallic active phases.

The catalytic activity of gold nanoparticles in CO oxidation reaction is known for a long time. In 1987, Haruta et al. showed that gold could be an active phase for oxidation reactions if present in nanoscale. CO conversion to  $\text{CO}_2$  by gold nanoparticles at low temperatures ( $-70^\circ\text{C}$ ) was demonstrated<sup>[40]</sup>. In cluster research, various experimental and theoretical studies of CO oxidation were performed to get insight into the reaction mechanism. Likely, gold nanoclusters have the highest activity when supported on ceria. This is due to two different mechanistic sources for oxygen. The first one is a Mars van Krevelen mechanism, where active oxygen is provided by  $\text{CeO}_2$ <sup>[41]</sup>. Good et al. found the coordination of lattice oxygen to be the rate limiting step<sup>[42]</sup>. Once the thiolate ligands are removed from the clusters by temperature treatment, the second mechanism comes into play<sup>[42]</sup>, which is a Langmuir Hinshelwood type. The combination of lattice and adsorbed oxygen provides ideal conditions for reactions of adsorbed carbon monoxide on the clusters. Partial removal of the ligands from the gold clusters also affects the activity in a positive or negative way<sup>[43,44]</sup>. Lopez-Acevedo et al. connected the catalytic activity of well defined thiolate protected gold nanoclusters with the HOMO-LUMO energy gap, which is associated with the binding of oxygen on the catalyst<sup>[45]</sup>. This quantum size effect is related to the number of electrons in the core that can be tuned either by number of atoms or introduction of dopants. Li et al. investigated the activity of bimetallic  $\text{M}_x\text{Au}_{25-x}(\text{SR})_{18}$  ( $\text{M}=\text{Cu}, \text{Ag}$ ) in CO oxidation<sup>[46]</sup> and found an enhancement effect in the doped samples compared to  $\text{Au}_{25}(\text{SR})_{18}$ . The oxidation of carbon monoxide is a well established model reaction in cluster research. Thus, it was implemented here for the investigation of catalytic property changes originating from cobalt dopants in  $\text{Au}_{25}(\text{SR})_{18}$  nanoclusters.



# Chapter II

## Motivation

The present Master Thesis is focused on the design and development of successful synthesis routes to obtain stable Co- and Co/Au-nanoclusters for the first time. Using various characterization techniques, their atomic structures, physical and chemical properties should be determined, aiming at applications in catalysis.

- Synthesis and characterization of stable monometallic thiolate protected cobalt clusters
- Synthesis and characterization of Co doped  $\text{Au}_{25}(\text{SR})_{18}$  clusters
- Determination of atomic structure, oxidation state, optical and chemical properties
- Study of catalytic activity in CO oxidation

# Chapter III

## Experimental

### III–1 Synthesis

#### 1 $\text{Co}_x(\text{SR})_m$ clusters

The synthesis of  $\text{Co}_x(\text{SR})_m$  clusters follows a modified Brust method<sup>[33]</sup>.  $\text{CoCl}_2 \cdot 6\text{H}_2\text{O}$  was dehydrated at  $150^\circ\text{C}$  to make it soluble in THF. To enhance the dehydration and to speed up the dissolving process the salt was grinded once during dehydration with a mortar and pestle. Progress is indicated by a color change from red to blue. Performing the synthesis in small batches leads to best results. 30 mg of  $\text{CoCl}_2$  were dissolved in 10 ml THF under vigorous stirring at room temperature. 100  $\mu\text{l}$  phenylethyl mercaptan were added. The color changed to dark blue or black. 80 mg of  $\text{NaBH}_4$  dissolved in ice cold  $\text{H}_2\text{O}$  were added for reduction. The reaction mixture was filtered and cleaned with methanol. The  $\text{Co}_x(\text{SR})_m$  clusters were recovered with DCM from the filter residue without allowing the reaction product to dry up at any time of the procedure. The pink  $\text{Co}_x(\text{SR})_m$  solution, that still contained impurities like methanol, was mixed with toluene. The solvent mixture was then striped from DCM under rotary evaporation leading to a two phase system. The Co clusters remained in the organic phase.

Table III.1: Reagents of  $\text{Co}_x(\text{SR})_m$  Synthesis

Reagent	quantity
THF	10 mL
$\text{CoCl}_2$	10 mg
2-PET	100 $\mu\text{l}$
$\text{NaBH}_4$	80 mg

## 2 $\text{Co}_x\text{Au}_{25-x}(\text{SR})_y$ Synthesis 1 (S1)

77.2 mg  $\text{HAuCl}_4 \cdot 3\text{H}_2\text{O}$ , 26 mg  $\text{CoCl}_2 \cdot 6\text{H}_2\text{O}$  and 700  $\mu\text{l}$  of the phase transfer catalyst Trihexyltetradecylphosphonium bromide (THTDPB) were mixed in 50 mL of  $\text{N}_2$  purged toluene and stirred for 3 h under inert atmosphere. Due to high humidity and the hygroscopic nature of the gold salt, it was not possible to quantitatively transfer  $\text{HAuCl}_4 \cdot 3\text{H}_2\text{O}$  from the weighing boats into the reaction flask. During stirring a color change from a golden to a greenish solution occurred. After 3 h the vast majority of  $\text{CoCl}_2 \cdot 6\text{H}_2\text{O}$  was dissolved and the thiol was added that led almost instantly to another change in color to a light blue. The radical starter azobis(isobutyronitril) (AIBN) was added to the reaction mixture in degassed toluene, but no reaction was apparent so the mixture was heated to  $80^\circ\text{C}$  and kept overnight, before it was reduced with 530 mg of  $\text{NaBH}_4$  dissolved in 10 mL of cooled Milli-Q water. The batch aged over night at room temperature resulting in a dark reddish brown solution. Toluene was evaporated and the precipitant was filtered and cleaned with ethanol several times. The product was dissolved in dichloromethane (DCM) leaving an insoluble black solid, similar to the  $\text{Co}_x(\text{SR})_m$  synthesis (III-1-1). Later DCM was substituted by toluene and stored at  $-20^\circ\text{C}$  over the weekend. Upon evaporation of toluene the same insoluble black precipitant formed again.

Toluene was evaporated and the clusters were dissolved in THF for SEC. The solution has divided into two parts. The faster eluting fraction of darker color did not seem to retard at all, thus a large particle size was expected.

Table III.2: Reagents of Synthesis S1

Reagent	quantity
Toluene	50 mL
$\text{HAuCl}_4 \cdot 3\text{H}_2\text{O}$	77.2 mg
$\text{CoCl}_2 \cdot 6\text{H}_2\text{O}$	26 mg
2-PET	500 $\mu\text{l}$
AIBN	100 mg
$\text{NaBH}_4$	530 mg
THTDPB	700 $\mu\text{l}$

## 3 $\text{Co}_x\text{Au}_{25-x}(\text{SR})_y$ Synthesis 2 (S2)

96 mg of Co- and 631 mg of Au salts were mixed and dissolved in 60 mL THF leading to a green solution. Since the solubility was very good for both, 1311 mg of

the phase transfer catalyst tetraoctylammonium bromide (TOAB) were added right after and stirred for 1 h at room temperature. The reaction flask was placed in an ice water bath and 1340  $\mu\text{l}$  thiol ligand were added. After 2 h 756 mg  $\text{NaBH}_4$  were added in 10 mL of cooled Milli-Q water resulting in a strong reduction reaction and a black solution. After a night of aging, THF was evaporated and methanol was added to precipitate the clusters and to remove unreacted thiols and side products. The suspension was filtered and redissolved in DCM, which then was evaporated again for a second cleaning step. The clean product was separated by solubility in acetonitril, acetone and DCM. Each fraction was divided individually by SEC in THF, since toluene did not provide a satisfying separation, until there was no change in the UV/Vis spectra.

Table III.3: Reagents of Synthesis S2

Reagent	quantity
THF	60 mL
$\text{HAuCl}_4 \cdot 3\text{H}_2\text{O}$	631 mg
$\text{CoCl}_2 \cdot 6\text{H}_2\text{O}$	96 mg
2-PET	1340 $\mu\text{l}$
$\text{NaBH}_4$	756 mg
TOAB	1311 mg

#### 4 $\text{Au}_{25}(\text{SR})_{18}$

$\text{Au}_{25}(\text{SR})_{18}$  was synthesized as reference material via the Brust method<sup>[33]</sup>. The reaction batch is shown in table III.4. Additionally,  $\text{Au}_{25}(\text{SR})_{18}$  fractions from the gold cobalt cluster synthesis that formed as side products, described in Chapter III-1-2 and III-1-3, were combined.

Table III.4: Reagents of  $\text{Au}_{25}(\text{SR})_{18}$  Synthesis

Reagent	quantity
$\text{HAuCl}_4 \cdot 3\text{H}_2\text{O}$	63 mg
TOAB	1312 mg
$\text{NaBH}_4$	530 mg
THF	60 mL
2-PET	500 $\mu\text{l}$

## III-2 Size exclusion chromatography (SEC)

Size exclusion chromatography was performed in a 1000 mm  $\times$  20 mm glass column with frit. The stationary phase was styrene divinylbenzene beads (Bio-Beads S-X1) from Bio-Rad. The clusters were separated with THF. Smaller clusters can enter pores of the stationary phase; therefore their elution path is longer than for large clusters, leading to shorter retention times for larger clusters. Cluster mixtures were dissolved in minimum amounts of THF and applied uniformly on top of the stationary phase. The column was run with about 20 drops/min.

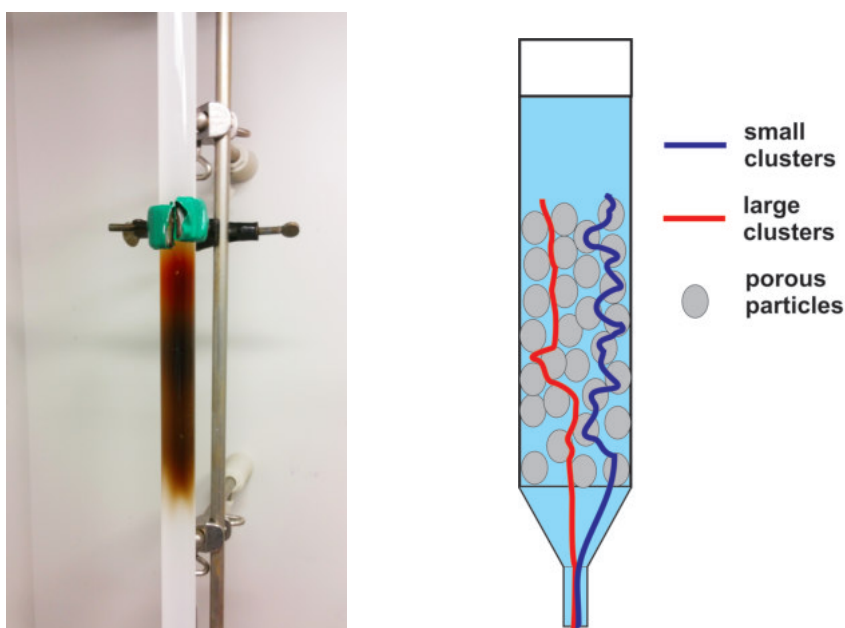


Figure III.1: Size exclusion chromatography (SEC)

## III-3 Catalyst preparation

Ceria was synthesized by combustion method<sup>[47,48]</sup>. Cerium nitrate and pluronic were dissolved in the minimum quantity of ethanol and heated in a muffle furnace in 10 °C min<sup>-1</sup> steps up to 300 °C and kept there for 4 h. The product was a flaky voluminous yellow ceria powder.

Table III.5: Reagents of CeO<sub>2</sub> combustion synthesis

Reagent	quantity
Cerium nitrate	11.48 g
Pluronic	0.2 g
Ethanol	

The catalysts were prepared by wet impregnation<sup>[49]</sup>. The support material CeO<sub>2</sub> was suspended in toluene. The clusters were also dissolved in toluene and added to the metal oxide suspension under vigorous stirring. After 12 h stirring the clusters had diffused into the pores of the metal oxide, leaving a suspension with a clear solvent. Toluene was removed under vacuum in a rotary evaporator.

Since the yields of the doped cluster syntheses were rather small, all fractions that contained Au and Co were combined and the atomic ratio was determined with grazing incidence x-ray fluorescence spectroscopy (see Chapter VI-1). In contrast, the gold catalyst was prepared with pure Au<sub>25</sub>(SR)<sub>18</sub> clusters only, leading to a very well defined reference.

## III-4 Characterization techniques

### 1 UV/Vis spectroscopy

UV/Vis spectra were recorded on a UV/VIS spectrometer (Perkin Elmer 750 Lambda) in transmission mode. Quartz cuvettes of 10 mm path length and the solvents dichloromethane and toluene were used.

### 2 MALDI

MALDI mass spectrometric measurements were performed using a prototype Axima TOF<sup>2</sup> MALDI time-of-flight (TOF)/reflectron (RTOF) mass spectrometer (Shimadzu, Kratos Analytical). For analytical experiments for Co 2,4,6-trihydroxyacetophenone (THAP, Sigma-Aldrich) and for Au trans-2-[3-(4-tert-butylphenyl)-2-methyl-2-propenylidene]malononitrile (DCTB, Sigma-Aldrich) were selected as MALDI-MS matrices. MALDI RTOF mass spectra of the cobalt clusters were acquired near threshold laser irradiance to obtain mass spectra of sufficient mass spectrometric resolution (3000 to 5000 at full width at half maximum (FWHM)). All displayed mass spectra were based on averaging 300 to 600 single and unselected laser pulses ( $\lambda = 337$  nm at 50 Hz). The MALDI measurements were done at the Institute of Chemical Technologies and Analytics at TU Wien in collaboration with Ernst Pittenauer.

### 3 Electron microscopy

High resolution transmission electron microscopy (HRTEM), high-angle annular dark-field (HAADF) imaging, as well as electron-energy loss spectroscopy (EELS) mapping and energy-dispersive X-ray spectroscopy (EDXS) were performed using a

200 kV FEI TECNAI F20 S-TWIN analytical (scanning) transmission electron microscope (S)TEM equipped with a Gatan GIF Tridiem filter. The energy resolution was  $\sim 1$  eV, the semi-convergence angle was  $\sim 8$  mrad, the semi-collection angle was  $\sim 15$  mrad and the spatial resolution was in the order of 0.5 nm. The measurements were performed in collaboration with Thomas Schachinger at USTEM TU Wien.

## 4 Raman spectroscopy

The Raman microscope system (Renishaw, System 2000; Yobin Yvon, LabRAM HR) consisted of a light microscope (Leica DL-LM; Olympus BX) coupled to a Raman spectrometer. The excitation laser was an Ar ion laser ( $k_0 = 514$  nm, source power 17 mW).

## 5 X-ray photoelectron spectroscopy (XPS)

X-ray photoelectron spectroscopy measurements were performed on a UHV system equipped with a Phoibos 100 hemispherical analyzer and a XR 50 X-ray source (all parts from SPECS GmbH). Spectra were recorded with Al- $K_\alpha$  radiation and data were analyzed with the CasaXPS software. Peaks were fitted after Shirley background subtraction with Gauss-Lorentz sum functions. Peak positions and full width at half-maximum (FWHM) were left unconstrained. For the S2p peak fitting, doublets with a fixed doublet separation of 1.2 eV (NIST XPS database) and a fixed area ratio of 2:1 were used for S2p $_{3/2}$  and S2p $_{1/2}$ . For the XPS measurements the clusters were drop-casted on a highly oriented pyrolytic graphite (HOPG) substrate and the solvent was evaporated by inserting the sample into the load lock chamber and applying vacuum for 4 h. This also allowed referencing the binding energies to the C1s signal of HOPG. The measurement was performed in collaboration with Christoph Rameshan.

## 6 Scanning Tunneling Microscopy (STM)

Scanning Tunneling Microscopy (STM) images of the nanoclusters were acquired with an Aarhus 150 STM from SPECS (for UHV-system see section III-4-5 (XPS)). A solution of the clusters was drop-casted on highly ordered pyrolytic graphite (HOPG) as support material. The HOPG with the nanoclusters was transferred to the STM chamber. The base pressure in the STM chamber was  $2.2 \times 10^{-10}$  mbar and the clusters were imaged with a Pt/Ir tip at 300 K. During the approach of the tip, a current of 0.35 nA and a tunneling voltage of 1.6 V was applied. For

image processing and line profile measurement the WSxM software was used. The measurements were performed in collaboration with Abhijit Bera.

## 7 Grazing incidence X-ray fluorescence analysis (GIXRF)

The atomic ratio of the catalysts was determined by GIXRF. A few grains of the catalyst were placed on a quartz reflector under the detector. A survey scan in x and y direction was performed already under vacuum. Once the optimum position was found, the sample was measured. To get enough signal from Co, a dead time of about 35 s was set because of the huge amount of CeO<sub>2</sub> as compared to gold and especially to cobalt. The mass percent and atomic ratios of the fitted XRF spectra were calculated by fundamental parameters. GIXRF measurements were performed on a home-made device at the Atominstitut (ATI) of TU Wien in collaboration with Dieter Ingerle<sup>[50]</sup>.

## III-5 X-ray absorption fine structure spectroscopy (XAFS)

XAFS is an X-ray absorption technique that analyses the fine structure around an specific adsorption edge. The sample is irradiated with increasing X-ray energy. When the energy of the incoming beam is equal to the binding energy of an electron, it gets ionized and knocked out of its shell. In the XANES energy region, which is directly around the adsorption edge, the electron scatters multiple times with surrounding neighbors, resulting in a specific shape and position of the so called white line, which contains information about oxidation state, symmetry, ligand configuration and chemical environment. At higher energies the effective cross section decreases, leading to a single scattering event. The electron wave scatters by its neighbor and interferes with the scattered wave. This phenomenon of superposition principle can be observed in the extended part of the absorption edge. From these oscillations distances between atoms and coordination number can be calculated with Fourier transformation.

X-ray absorption spectroscopy measurements were carried out at the XAS beamline at Elettra-Sincrotrone Trieste (Italy) and at the SuperXAS beamline at the Swiss Light Source (Switzerland). S K-edge (2472 eV) was measured at Elettra-Sincrotrone using a Si (111) double-crystal monochromator. The photon flux was about 10<sup>9</sup> photons/s. Experiments were performed in fluorescence mode using a silicon drift detector (Oxford Instruments). A concentrated solution of the sample was drop-casted onto a sulfur-free polyimide (Kapton) tape and mounted



on an in-house made cell (Section III-7) of working under high vacuum and at liquid nitrogen temperature. XANES at Co K-edge (7709 eV) was measured at Swiss Light Source. The incident photon beam provided by a 2.9 T Super Bend magnet was selected by a Si(111) channel-cut monochromator. The rejection of higher harmonics and focusing were achieved by a Si-coated collimating mirror at 2.8 mrad and a rhodium-coated toroidal mirror at 2.8 mrad. The size of the X-ray beam on the sample was  $0.3\text{ mm} \times 0.3\text{ mm}$  with a total intensity of about  $5 \times 10^{11}$  ph/s to  $7 \times 10^{11}$  ph/s. Fluorescence signal was detected with five-element SDD detector (SGX). A concentrated solution of the sample in toluene was placed in a quartz capillary and cooled down with a cryo-gun to liquid nitrogen temperature. The data analysis was performed according to standard procedures using Ifeffit software<sup>[51]</sup>.

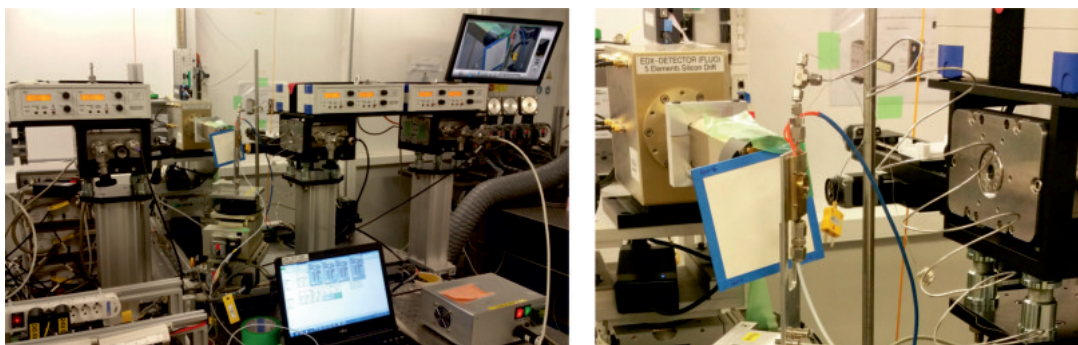


Figure III.2: XAFS in-situ reaction setup (SLS)

## III-6 In-situ DRIFTS measurements

Diffuse reflectance infrared Fourier transform spectroscopy (DRIFTS) was performed on a VERTEX 70v. The open drift cell together with the reactor cell, which is described in section III-7 for the in-situ measurements, is shown on the right side of Figure III.3. On the left side is a front view with three different gas lines. One oxidation line for  $\text{O}_2/\text{Ar}$ , a reduction line for  $\text{CO}/\text{Ar}$  and the mainline with pure Ar. The valves are switched electronically. The Setup for in-situ DRIFTS measurements is described more detailed in Chiarello et al.<sup>[52]</sup>.

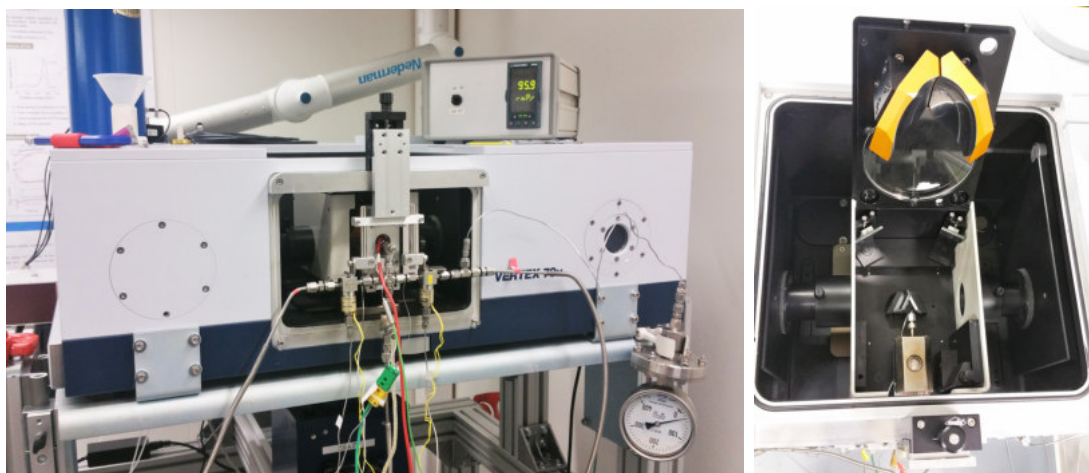


Figure III.3: DRIFTS in-situ reaction setup (PSI)

### III-7 Catalytic activity tests

For the catalytic studies with CO oxidation as model reaction, a reactor setup was used, which was developed in the group of Davide Ferri<sup>[52]</sup>. The reaction cell and its components are shown in Figure III.4. There are gas inlets and outlets for gas reaction, heat cartridges for TPR and two windows for different spectroscopic techniques like DRIFTS, XAFS or XRD.

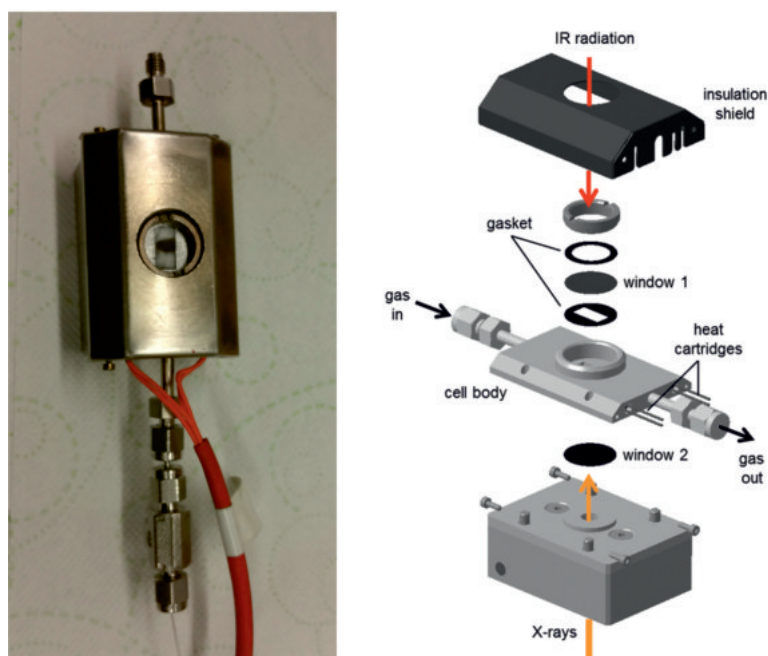


Figure III.4: Left: Reactor cell filled with catalyst. Right: Exploded view of reactor cell. Adapted from Chiarello et al.<sup>[52]</sup>.

## 1 Cell preparation

To guarantee stable experimental conditions, without loss of catalyst through gas in- and outlets of the cell, the material was pressed into pellets with a pressure of  $1 \text{ t cm}^{-2}$  first and was then carefully tapped and sieved. For the cell, particles collected between 100 and 150  $\mu\text{m}$  of mesh width were taken. Furthermore, the gas in- and outlets of the cell were blocked for particles with quartz wool by placing the fibers perpendicularly in front. The catalyst was placed in the center of the cell, with the smallest amount of quartz wool possible between the catalyst and the  $\text{CaF}_2$  window. Graphite foil was used to seal the backside of the cell to the heating block.

For XAFS analysis a similar but thinner cell was used, holding two graphite windows.

Pretreatment of the catalyst was done in oxidative conditions for each reaction separately: by using 5 % of Oxygen in Argon with a total flow of 50 mL/min directly in the reactor cell. The cell was heated in  $5^\circ\text{C}/\text{min}$  steps to a maximum temperature of  $150^\circ\text{C}$  and kept there for 30 min. After this process the cell was cooled with pure Argon to less than  $40^\circ\text{C}$ . Immediately after the pretreatment the gas flow was changed to a ratio of 1:1 of CO and  $\text{O}_2$ , which supplies twice as much oxygen as CO for the reaction. Again, a total gas flow of 50 mL/min was used with 1 % of reagents and 99 % Argon. For the kinetic studies a temperature program for heating to the maximum temperature and cooling down afterwards at  $5^\circ\text{C}/\text{min}$  steps was run to check for hysteresis in the conversion. The reaction was followed by in-situ DRIFTS and mass spectroscopy. The most promising catalysts were investigated with XAFS later on.

# Chapter IV

## $\text{Co}_x(\text{SR})_m$ cluster

For the first time stable monolayer protected thiolated cobalt nanoclusters were synthesized by a wet chemical method, leading to a pink solution with well-defined optical activity (UV/Vis) and photoluminescence (PL). The cobalt cluster core of around 1.3 nm size was metallic (as indicated by STEM, STM, XPS, HAADF-EELS) and was surrounded by a specific configuration of thiolate staples (according to Raman, FTIR, XAFS, MALDI) that is similar to that of corresponding gold clusters.

The clusters exhibit characteristic UV/Vis spectra and optical properties. The staple configuration of  $-\text{S}-\text{metal}-\text{S}-$ , typical of thiolate protected gold clusters, was also observed in the case of the cobalt clusters, maintaining the cobalt atoms in the metallic state.

Results of the  $\text{Co}_x(\text{SR})_m$  studies of this thesis were published in Pollitt et al.<sup>[53]</sup>.

### IV-1 Synthesis of $\text{Co}_x(\text{SR})_m$ clusters

The synthesis strategy of the thiolated cobalt clusters was based on previous synthesis routes of monometallic and bimetallic thiolated gold clusters. However, in light of the comparably easier oxidation of cobalt and, thus, the difficulty to synthesize stable metallic cobalt clusters with a narrow range of particle size, several optimization steps had to be applied. TOAB (tetrabutylammonium bromide), which acts as a phase-transfer catalyst, is commonly used in the synthesis of thiolate protected gold clusters  $\text{Au}_n(\text{SR})_m$ . It improves the solubility of metal salts in organic solvents, which facilitates the reaction. Nevertheless, this kind of quaternary ammonia compounds have a high tendency to oxidize cobalt, which makes the synthesis of metallic cobalt clusters difficult. TOAB was not used for this synthesis, instead the hydrated metal salt precursor was dried, which also improved the solubility in THF, since cobalt then forms a complex with THF, which is replaced by the thiolate

ligands via a ligand exchange reaction<sup>[54]</sup>. Since the formation of this starting complex is only possible with  $\text{Co}^{2+}$ , the (further) oxidation of cobalt should be avoided. Thus, for cobalt cluster synthesis short reaction times are beneficial to obtain a higher yield of metallic Co. This is due to the tendency of THF to form peroxides that on one hand are radical starters but on the other hand oxidize cobalt. In contrast, for the synthesis of thiolated gold clusters, longer aging times lead to narrower size distribution, because only the most stable structures remain.

Following these directions, a pink product was obtained. In order to separate different cluster sizes, the sample was passed through a size exclusion chromatography (SEC) column<sup>[55,36]</sup> until a unique single fraction with characteristic and well-defined UV/Vis spectrum was obtained as discussed in Chapter IV-2-4. The synthesis was repeated several times, each time reproducibly leading to the same highly stable product when dissolved in DCM or toluene. Once the sample was dried (powder form) and after some air exposure it got oxidized to an insoluble black precipitate. Finally, a precise and reproducible synthesis route was developed, yielding to stable thiolate protected cobalt clusters for the first time.

## IV-2 Characterisation of $\text{Co}_x(\text{SR})_m$

### 1 MALDI-TOF-MS

For studies of the composition of thiolated metal clusters, MALDI-TOF-MS is the most frequently applied technique. In the case of Au clusters, trans-2-[3-(4-tert-butylphenyl)-2-methyl-2-propenylidene]malononitrile (DCTB) was found as an optimal matrix, with a low degree of metal cluster fragmentation. In the case of cobalt clusters using a DCTB matrix led to a higher degree of fragmentation in the low  $m/z$  range, even under lower laser irradiance, similar as observed before for thiolated iridium clusters<sup>[19]</sup>. After screening different matrices, 2,4,6-trihydroxyacetophenone (THAP) led to a lower degree of fragmentation and to reproducible results for the synthesized thiolated cobalt clusters. Figure IV.1 shows the MALDI TOF mass spectrum obtained from  $\text{Co}_x(\text{SC}_2\text{H}_4\text{Ph})_m$  in positive ion mode.

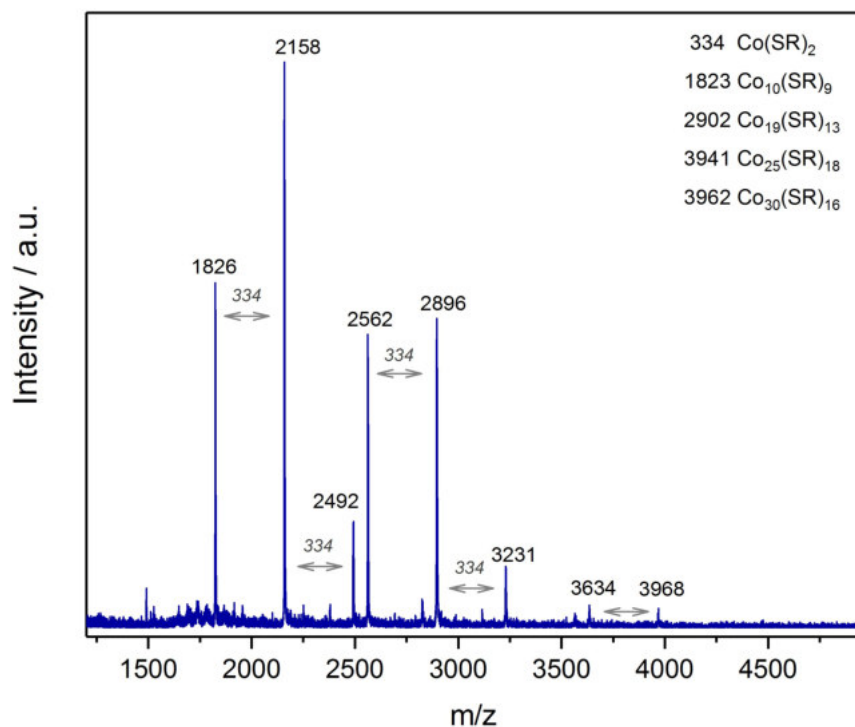


Figure IV.1: MALDI-TOF-MS spectrum of the prepared  $\text{Co}_x(\text{SR})_m$  clusters.

The analysis of the mass spectrum revealed a difference of  $m/z=334$  between the major peaks, which corresponds to the  $\text{Co}(\text{SR})_2$  unit which is a monometallic staple. The same type of characteristic fragment was also observed in MALDI mass spectra of thiolated gold clusters. The range of observed masses were between  $m/z=1826$  and  $m/z=3968$ . The higher one seems related to clusters containing  $\text{Co}_{30}(\text{SR})_{16}$ , but due to the high degree of fragmentation it was not possible to assign a specific formula or structure. The MALDI-MS results suggest formation of cobalt clusters in a range of 25 to 30 Co atoms, with a clear fragmentation pattern of staple motifs (-S-Co-S-) in Figure IV.2, which are characteristic of thiolate protected metal clusters.

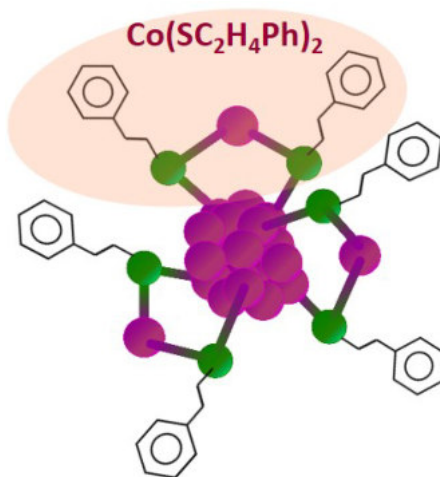


Figure IV.2: Staple motif of Co-clusters. Co (magenta), S (green)

Several groups, such as Tsukuda, Dass, Murray or McLean, have analyzed thiolate protected clusters by MALDI- and ESI-MS, reporting this kind of staple fragmentation, with the capping structures directly desorbing from the Au-nanoparticle surface. The crystallographically characterized  $\text{Au}_2(\text{SR})_3$  staples of the  $\text{Au}_{25}(\text{SR})_{18}$  cluster have also been observed by ESI-MS/MS, which represents the long staple configuration only<sup>[56,57,58,59,60,61,62]</sup>.

## 2 TGA

In order to obtain complementary insight on cluster composition, thermogravimetric analysis (TGA) was performed. The TGA profile in Figure IV.3 shows a weight loss of 59 % between 75 °C and 375 °C that is related to the complete removal of the thiolate ligands ( $-\text{SC}_2\text{H}_4\text{Ph}$ ). The higher range of  $m/z$  observed by MALDI-MS, i.e.  $\text{Co}_{25}(\text{SR})_{18}$  and  $\text{Co}_{30}(\text{SR})_{16}$  clusters, would exhibit a weight loss related to ligands of 62 % and 55 %, respectively. Thus, the 59 % weight loss observed for the synthesized cobalt clusters is in good agreement with that expected from the cobalt cluster compositions determined by MALDI. However, three steps were observed during the ligand removal process; weight losses of 8 % at lower temperature (75 °C to 150 °C), a main weight loss of 41 % at 150 °C to 290 °C, and 10 % loss at higher temperature (290 °C to 375 °C). Previous studies on thiolated gold clusters have also reported different weight loss steps that were ascribed to different staple configurations (long and short staples), but also to the interaction of the oxidative atmosphere with thiol ligands that may lead to different removal processes. These may explain the two higher temperature steps for cobalt clusters. Carotenuto et al. studied the thermal stability of cobalt thiolates ( $\text{Co}-\text{C}_{18}\text{H}_{37}\text{SH}$ ) and also reported weight losses at 260 °C

and 360 °C<sup>[21]</sup>. Thus, the low temperature step may be due to oxide species attached to the cluster, which are discussed in Chapter IV–2, section 7 and 8.

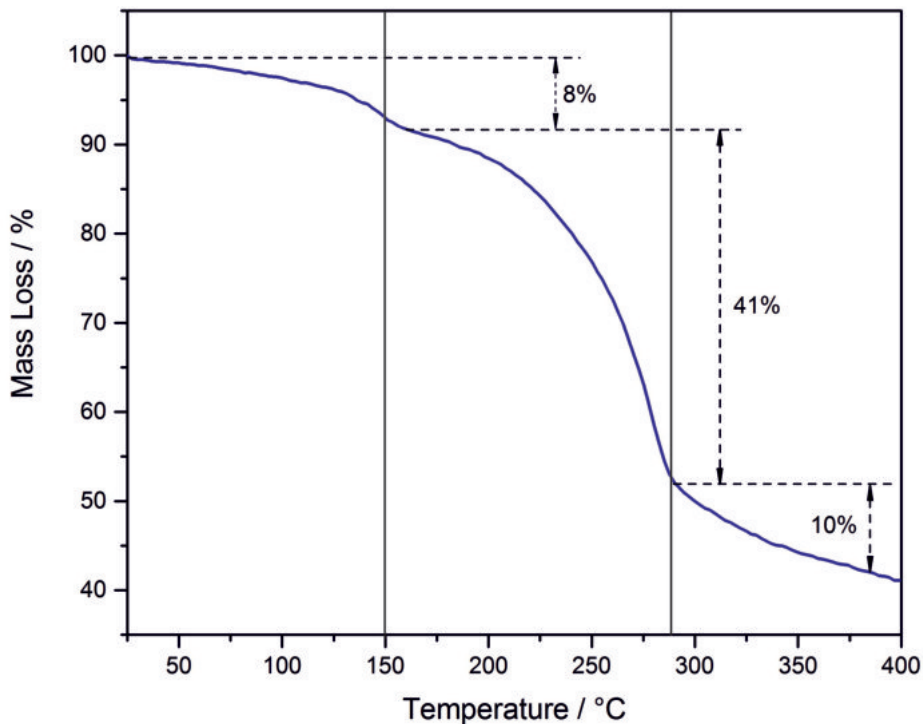


Figure IV.3: Thermogravimetric analysis of  $\text{Co}_x(\text{SC}_2\text{H}_4\text{Ph})_m$  clusters.

### 3 XRD

X-ray diffraction measurements were performed to confirm the formation of Co cluster and to discard  $\text{CoS}_x$  complexes or larger Co nanoparticles, which exhibit highly crystalline structures, as reported in literature<sup>[21,63,64]</sup>. As shown in Figure IV.4, XRD revealed that the samples were not crystalline. Few small diffraction reflexes appear under the retardation spectrum coming from amorphous material. Reflexes at 18 and 28.5  $2\theta$  are from DCM, which was incorporated during dropcasting of the clusters on the sample holder for the measurement. Bond distances were calculated from the  $2\theta$ -positions of the reflexes. The calculated values did not match the values of fcc and hcp Co. (fcc:  $a=2.5 \text{ \AA}$ , hcp:  $a,b=2.5 \text{ \AA}$ ,  $c=4 \text{ \AA}$ ). The diffraction pattern also did not match any other compound from the pdf-4(2016) database.



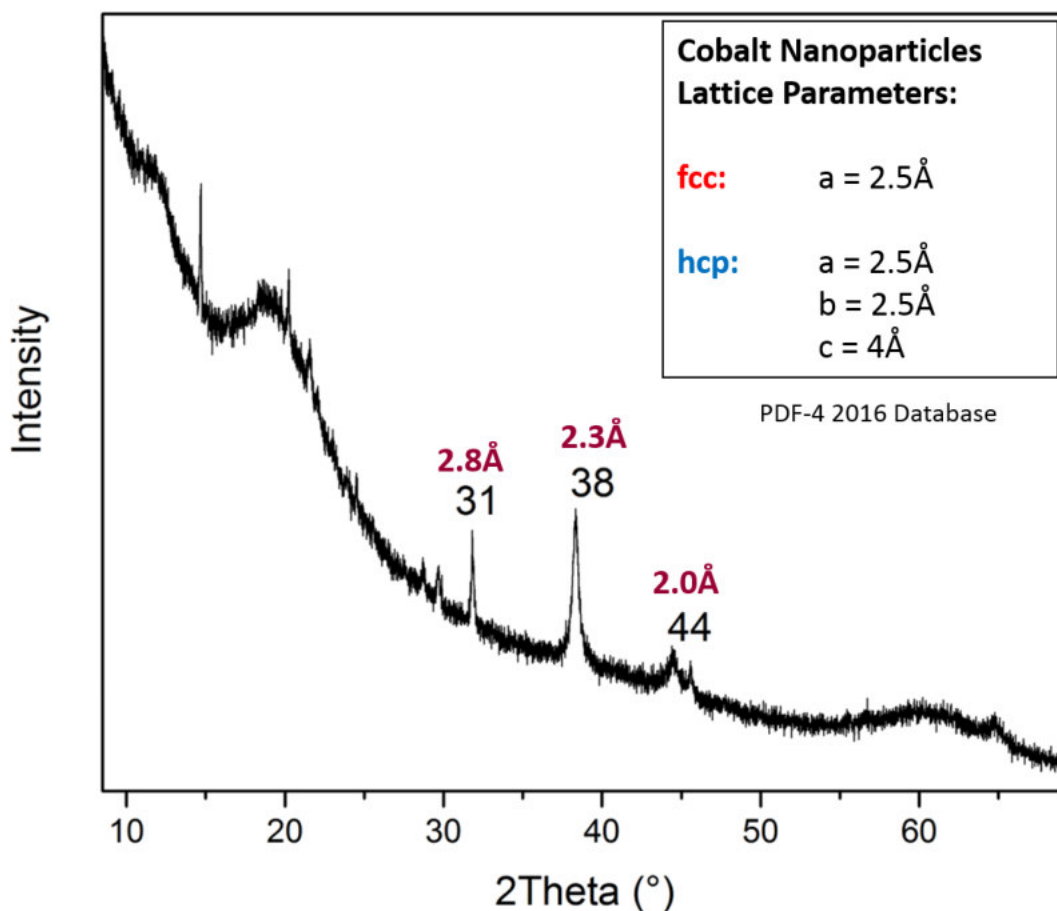


Figure IV.4: Comparison between Co-clusters and bulk Co with X-ray powder diffraction.

#### 4 UV/Vis and Photoluminescence Spectroscopy

Due to their molecule-like electronic structure, atomic scale metal nanoclusters exhibit one or more absorption peaks in UV/Vis, in contrast to the surface plasmon resonance (SPR) band observed for larger particles. UV/Vis absorption spectra of the synthesized cobalt clusters dissolved in dichloromethane (DCM), shown in Figure IV.5, exhibit four main absorption peaks at 311, 413, 505 and 639 nm.

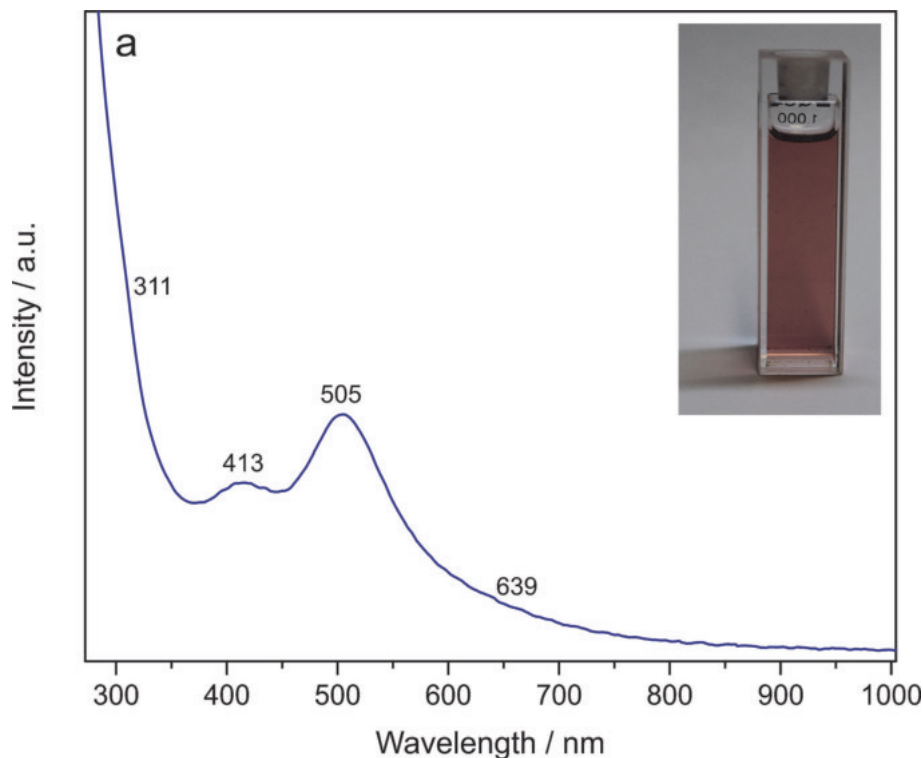


Figure IV.5: UV/Vis spectrum of Co clusters in dichloromethane.

A comparison with the characteristic SPR band of larger Co nanoparticles is not straightforward due to conflicting reports in literature. Based on Mie's theory, calculations and experimental studies expect very weak absorption in the range of 250 nm to 450 nm (285 nm<sup>[65]</sup>, 360 nm and 495 nm<sup>[66]</sup>) and in the range of 497 nm to 520 nm<sup>[22]</sup> (520 nm<sup>[67]</sup>), but all reports agree that SPR is represented by a very broad band. Thus, the formation of clusters is evidenced by the defined (and not broad) absorption bands at different wavelengths. In order to compare the cobalt clusters with common cobalt nanoparticles, the latter were prepared according to reported methods<sup>[21,22]</sup>, with an additional passivation step with the same thiolate ligand (-SC<sub>2</sub>H<sub>4</sub>Ph). The particles are stable only for short time and form an insoluble black precipitate. Nevertheless, a comparison of UV/Vis spectra of short-living cobalt nanoparticles in DCM and of Co<sub>x</sub>(SR)<sub>m</sub> clusters is shown in Figure IV.6. For nanoparticles bands are broader and shifted.

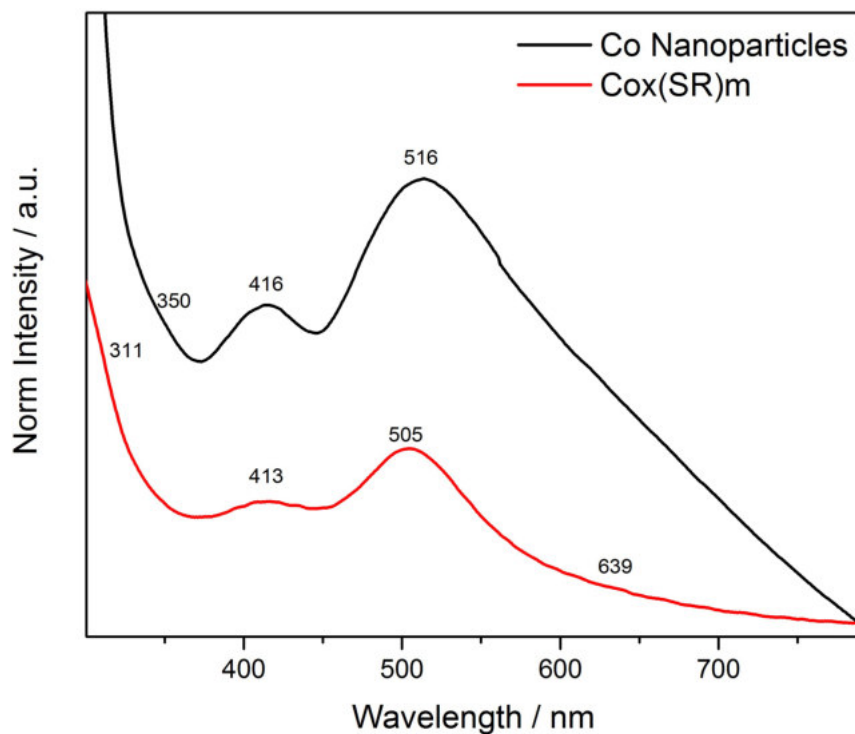


Figure IV.6: Comparison of UV/Vis spectra of Co nanoparticles (with  $\text{SC}_2\text{H}_4\text{Ph}$  ligands) and  $\text{Co}_x(\text{SC}_2\text{H}_4\text{Ph})_m$  clusters dissolved in dichloromethane.

Figure IV.7 shows the photoluminescence spectrum of the cobalt clusters. The emission spectrum upon excitation at 412 nm shows intense luminescence peaks at the blue and yellow region, with two emission peaks in 475 nm and 575 nm. The observed dual fluorescence is a typical indicator of charge transfer occurring in the clusters upon excitation. Previous studies on glutathione-protected gold clusters also displayed such dual luminescence<sup>[68,69,70]</sup>, which was explained by Whetten et al.: the high energy luminescence being an inter-band transition from excited states in the sp-band to the d-band<sup>[71]</sup> and the low energy as the intra-band HOMO-LUMO transition within the sp band. However, complementary calculations and studies would be required to explain the origin of the dual luminescence of cobalt clusters.

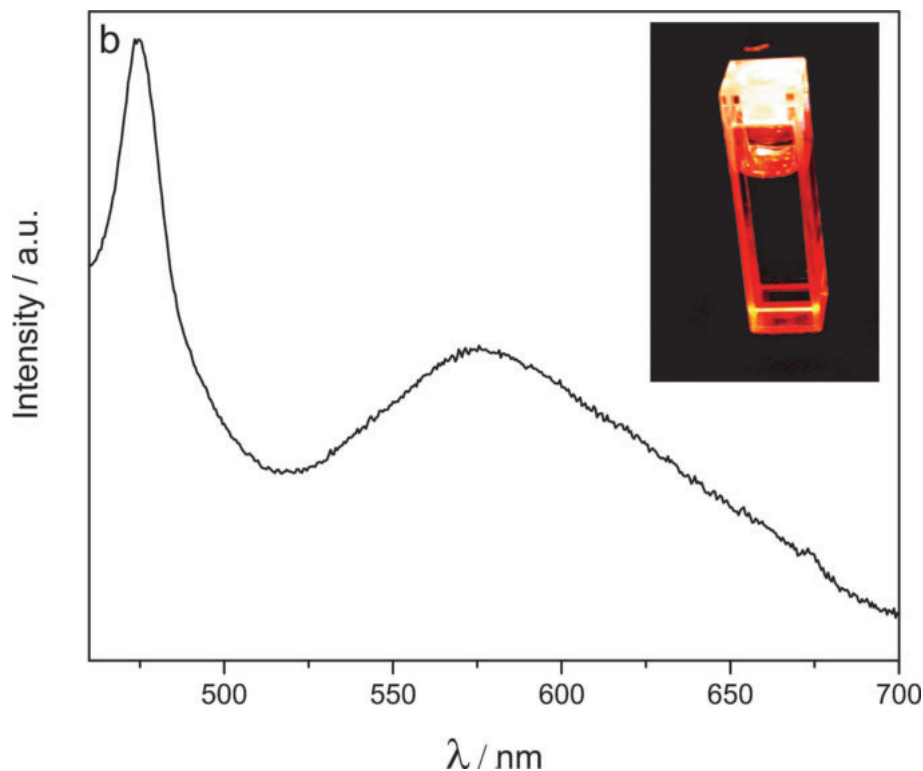


Figure IV.7: Photoluminescence spectrum of Co clusters. Co clusters in dichloromethane solution are shown as inset, with UV/Vis illumination ( $\lambda$  from 220 nm to 400 nm).

## 5 Electron Microscopy

The STEM picture (Figure IV.8) shows uniform cobalt clusters with an average particle diameter of around 2 nm. EELS analysis at the Co  $L_3$  edge indicated a tendency of the Co  $L_3$  edge to shift to lower energies at the center of the cluster, and to higher energies at the cluster edge, which would point to metallic Co at the center and a partially oxidized perimeter<sup>[72,73]</sup>. The oxidation may occur during deposition onto the TEM grid. The EDX spectrum in Figure IV.9 shows mainly carbon, sulfur and cobalt, but a minimal content of oxygen. Figure IV.10 shows the EELS mapping of the region that is indicated by a green rectangle, displaying the signal maps of carbon, sulfur and cobalt. Figure IV.11 shows the energy loss spectrum of the clusters versus a metallic reference.

The onset of the Co  $L_3$  edge of the sum spectrum of the EELS mapping indicated metallic Co atoms<sup>[72,74]</sup>, in agreement with the selected area electron diffraction (SAED) pattern in Figure IV.12.

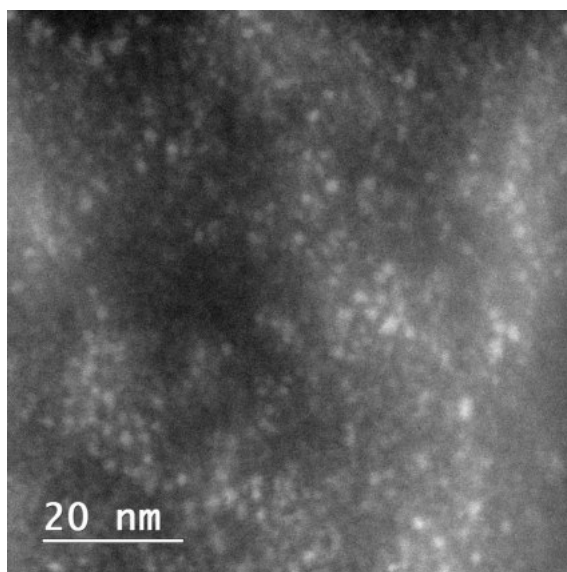


Figure IV.8: STEM image of  $\text{Co}_x(\text{SR})_{18}$

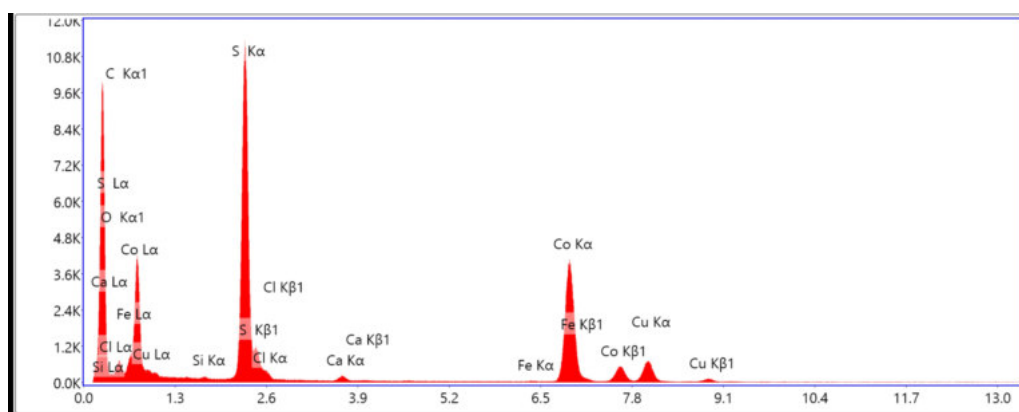


Figure IV.9: EDX spectrum of Co nanoparticles

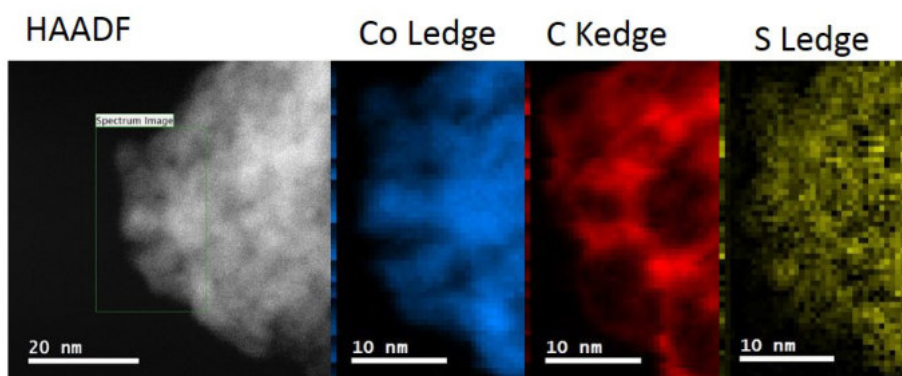


Figure IV.10: HAADF with EELS mapping region. Co L-edge signal map (blue), C K-edge (red), S L-edge (yellow)

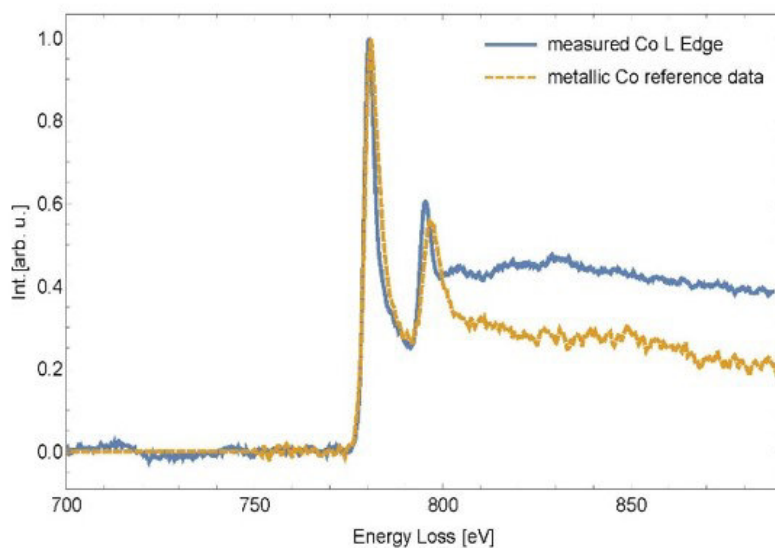


Figure IV.11: EELS Co L<sub>3</sub> spectrum showing metallic Co

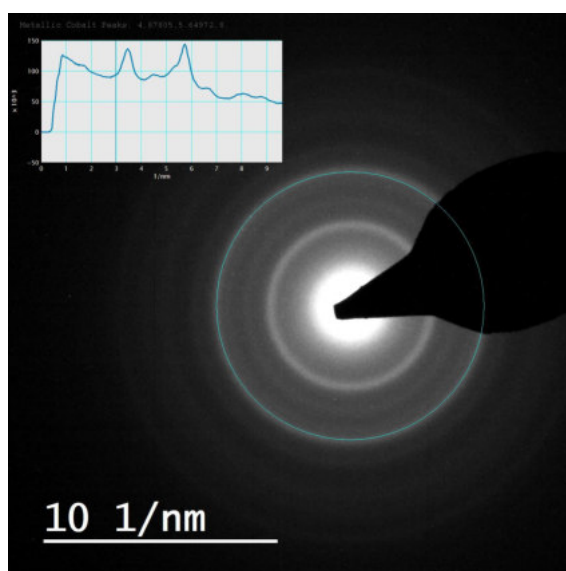


Figure IV.12: SAED

## 6 STM

In order to corroborate the structure and size information, room temperature STM measurements were performed. Figure IV.13 shows clusters with roughly spherical shape, deposited on highly ordered pyrolytic graphite (HOPG). HOPG was chosen as substrate surface as it is atomically flat and clean, which facilitates the detection of nanoclusters and reliable measurements of cluster size and height. Cluster size analysis via line profiles indicated an average size of 1.3 nm and 1 nm height (Figure IV.14). Atomic resolution of the clusters was not obtained, likely due to the insulating character of the ligands and the sample temperature of 300 K.

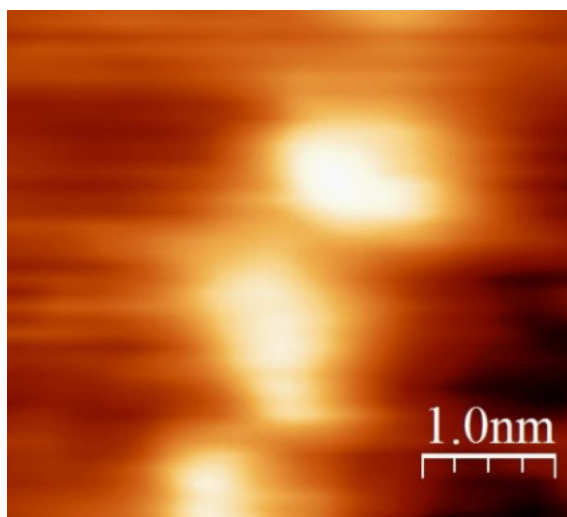


Figure IV.13: STM image of Co clusters supported on HOPG, taken at room temperature ( $V_{\text{sample}}=1.6\text{ V}$ ,  $I_{\text{tunnel}}=0.35\text{ nA}$ ). The cluster size is around 1.3 nm.

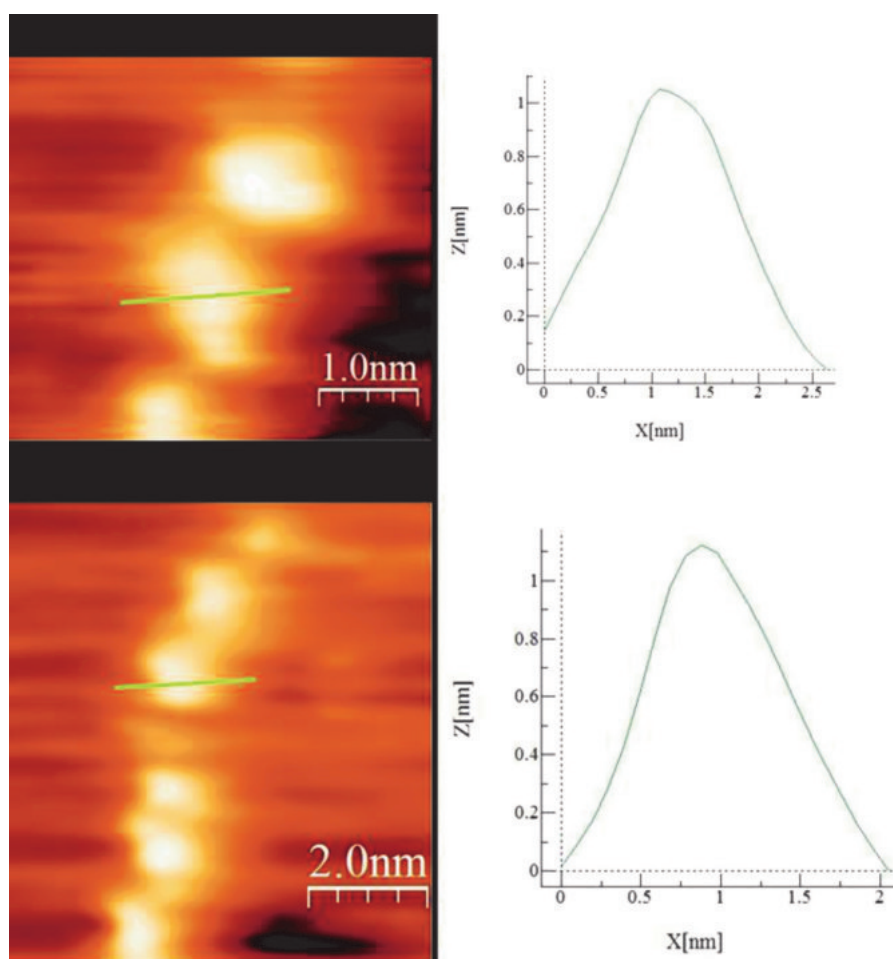


Figure IV.14: STM topography and corresponding line profiles of cobalt clusters on HOPG.

## 7 Vibrational Spectroscopy

Vibrational Spectroscopy is a useful technique for studying molecular conformation and properties of nanomaterials. The Raman spectra of the synthesized  $\text{Co}_x(\text{SR})_m$  clusters in the range of  $200\text{ cm}^{-1}$  to  $2000\text{ cm}^{-1}$  on the left side in Figure IV.15 shows characteristic peaks at higher energies, an intense peak at  $1100\text{ cm}^{-1}$  related to the bonded thiolate ligands ( $-\text{SC}_2\text{H}_4\text{Ph}$ ) and another around  $1420\text{ cm}^{-1}$  related to the aromatic ring. Based on previous Raman studies of metal sulfides, the peaks between  $200\text{ cm}^{-1}$  to  $450\text{ cm}^{-1}$  can be attributed to Co–S vibrations, with a prominent band around  $350\text{ cm}^{-1}$ <sup>[23]</sup>. The right side of Figure IV.15 displays a spectrum of the  $\text{Co}_x(\text{SR})_m$  clusters in the low wavenumber region, with a broad peak at  $322\text{ cm}^{-1}$  and a smaller one at  $419\text{ cm}^{-1}$ , assigned to Co–S vibrations in agreement with previous studies<sup>[23,75,76,77]</sup>. The comparison of Raman spectra of the prepared  $\text{Co}_x(\text{SR})_m$  clusters with those reported for different  $\text{CoS}_x$  compounds (nanostructures, complexes, etc.) revealed pronounced differences of the vibrational bands (Raman shifts) and relative intensities. However, when the Raman spectra of cobalt clusters are compared to those of monolayer protected thiolated gold clusters, several similarities are apparent<sup>[78,79,80,81]</sup>. Thiol ligands in similar environments or configurations like in the staple bonds should exhibit similar vibrational properties for Co and Au, but the frequencies may be slightly shifted due to different masses and force constants.

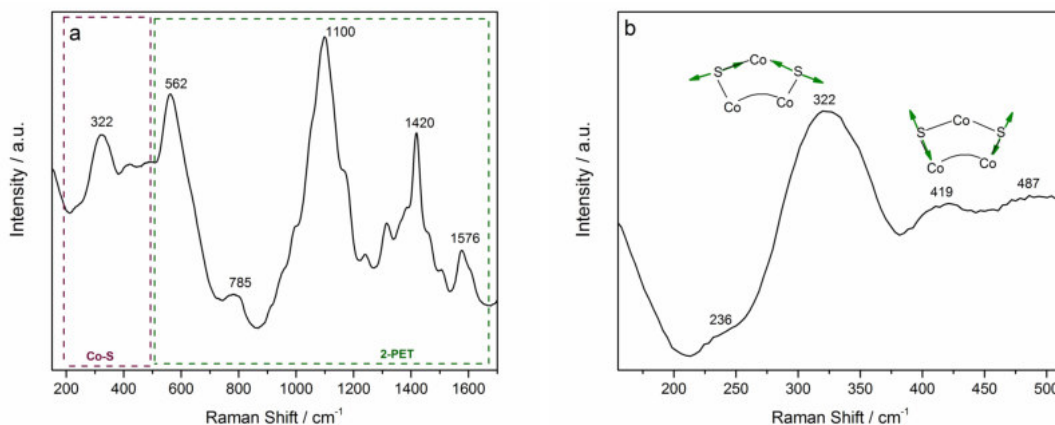


Figure IV.15: Raman spectra of  $\text{Co}_x(\text{SR})_m$

Raman spectroscopy of gold clusters have focused on the Au–S interface and both experimental and theoretical studies were reported<sup>[82,83,84,85]</sup>. Two types of Au–S stretching vibrations can be distinguished in the lower wavenumber range of  $200\text{ cm}^{-1}$  to  $350\text{ cm}^{-1}$ , related to Au(core)–S in radial mode and to Au(staple)–S in tangential mode bonds. Different radial vibrations were observed depending on the type of staples. Short staples lead to vibrations at lower energies and for the bending of longer staples higher energy is required.



The Co-S vibrational band is again expected to be shifted with respect to Au-S, based on the smaller mass of Co in relation to Au, which should lead to a shift to high frequency. However, the binding strength in Co-S is weaker than in Au-S, leading to a shift to lower frequency. In total, the two effects compensate each other and the Co-S band and Au-S band are similar. According to Raman studies of the Au-S vibration related to the staple configuration<sup>[83]</sup>, the presence of a single strong peak at  $322\text{ cm}^{-1}$  can be attributed to the Co-S bond in the short staples, in agreement with the fragmentation pattern observed by MALDI-MS. The radial mode vibrations were reported for higher energies with low intensity (due to the movement of the thiolate against the cluster surface), and the small peaks between  $400\text{ cm}^{-1}$  and  $500\text{ cm}^{-1}$  may thus be assigned to the Co(core)-S bonds.

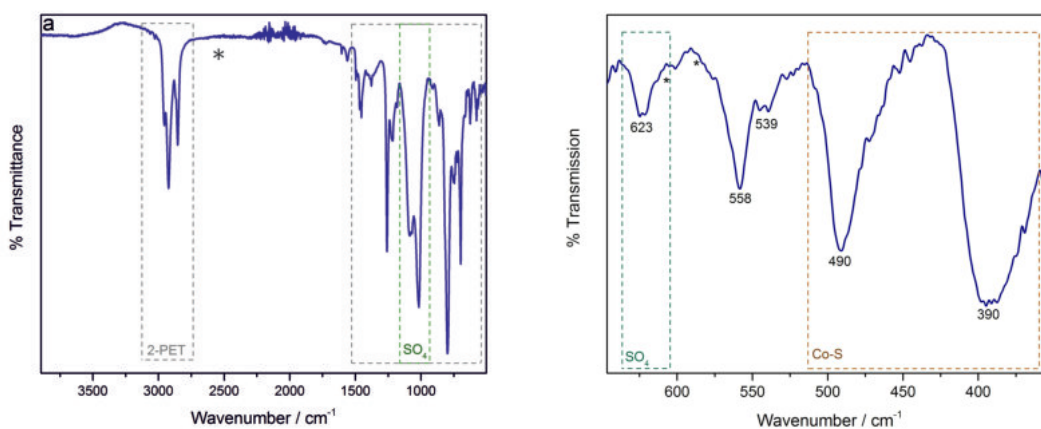


Figure IV.16: Left: MIR; Right: FIR FTIR spectra of  $\text{Co}_x(\text{SR})_m$  clusters.

For further structural characterization mid- and far-infrared FTIR measurements were performed. The spectrum in the left side of Figure IV.16 confirms the bonding between Co and S by the absence of the S-H stretching vibration, expected around the marked position (\*) of  $2525\text{ cm}^{-1}$  in the MIR spectra, whereas the characteristic C-H, C-S and aromatic stretching bands of the  $(-\text{SC}_2\text{H}_4\text{Ph})$  ligand were indeed observed. In addition, the spectrum shows an unexpected strong band at  $1000\text{ cm}^{-1}$  to  $1200\text{ cm}^{-1}$ . Based on literature, S=O stretching bands of sulfur oxide compounds produce strong infrared bands in the  $1400\text{ cm}^{-1}$  to  $1000\text{ cm}^{-1}$  range. The right side of Figure IV.16 shows the FIR region, also displaying a band at  $623\text{ cm}^{-1}$  that may be assigned to the asymmetric bending of the  $\text{SO}_4$  groups, typically found between  $600\text{ cm}^{-1}$  to  $640\text{ cm}^{-1}$ . Thus, the bands observed in the MIR spectra confirm the presence of sulfur oxide species. The band around  $550\text{ cm}^{-1}$  is related to mercaptan compounds, in this case the thiol ligand. The bands observed between  $350\text{ cm}^{-1}$  and  $500\text{ cm}^{-1}$  further confirm the Co-S bond.

## 8 XPS

XPS analysis was performed to determine the oxidation state of the cobalt clusters. The left side of Figure IV.17 shows the Co  $2p_{3/2}$  region, including peak fitting. The 779.6 eV signal is attributed to metallic cobalt from the clusters. Similarly to monolayer protected Au-clusters the binding energy Co-clusters is 1.5 eV higher than bulk metallic Co<sup>[86]</sup>. Zhang showed for decreasing size of Au(SR) nanoparticles that the Au 4f peaks shift to higher binding energy<sup>[87]</sup>. This shift results from a nanosize effect and from surface metal–ligand interactions in the nanoparticles<sup>[87]</sup>. The signal at 781.6 eV can be attributed either to the cobalt–sulfur bond or to cobalt oxide (CoO). The observed plasmon feature at  $\sim 785$  eV fits both Co–S and CoO. In comparison, Co<sub>3</sub>O<sub>4</sub> is missing the plasmon feature<sup>[86,88]</sup>. Tao et al. and Ganesan et al. reported binding energies (BE) of 781.4 and 781.3 eV for cobalt sulfide nanoparticles, respectively<sup>[64,89]</sup>. Due to the nanosize effect also the binding energy of CoO may be shifted by 1.5 eV to higher BE. However, an unambiguous assignment of the 781.6 eV feature to either Co–S or CoO would require additional high–resolution measurements. Nevertheless, the additional results from SAED, Raman and XAFS indicate Co–S bonds rather than Co–O.

In the S 2p spectrum on the right side of Figure IV.17 the signal comprises three components, at 162.4, 164.7 and 168.2 eV. As this is the first report of synthesis of protected cobalt clusters, there are no reference data but only studies of self-assembled monolayers (SAM) of metallic cobalt provide useful results for S 2p. The peak at 162.4 eV can be attributed to the sulfur–cobalt bond, in agreement with values for S–Co of SAMs ( $\sim 162.5$  eV, dodecanethiol), reported by Devillers et al.<sup>[90]</sup> and (168.2 eV, octadecanethiol) by Pookpanratana et al.<sup>[91]</sup>. The peak at 168.2 eV can be attributed to fully oxidized sulfur. Once more, this agrees with the results of Devillers et al. which reported oxidation of sulfur ( $\sim 168.5$  eV) in the SAMs, when the surface was not fully covered and oxygen reacted with the SAM. Similarly, Pookpanratana et al. reported fully oxidized sulfur at  $\sim 168.6$  eV. Further, partially oxidized sulfur is present, corresponding to the S2p signal at 164.7 eV<sup>[92]</sup>.

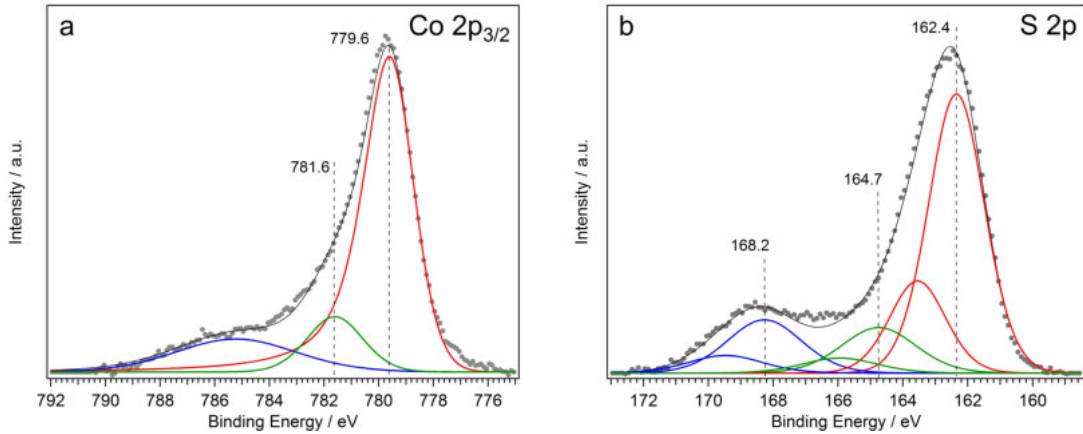


Figure IV.17: (a) XPS spectra of the Co  $2p_{3/2}$ ; (b) the S  $2p_{3/2}$  and S  $2p_{1/2}$  core level shifts of the  $\text{Co}_x(\text{SR})_m$  clusters on HOPG.

## 9 XAFS

The electronic structure and the local chemical environment of the  $\text{Co}_x(\text{SR})_m$  clusters were studied by X-ray absorption near edge spectroscopy (XANES) at the Co K-edge and S K-edge and compared to the following reference samples: Co foil, CoO, thiol ligand(2-PET),  $\text{SO}_2$ ,  $\text{SO}_3$  and  $\text{SO}_4$ . The spectra are shown in Figure IV.18. In case of Co K-edge XANES spectra, the high intensity of the white line, the edge position and the broad white line feature for  $\text{Co}_x(\text{SR})_m$  clusters – when compared to the reference materials - suggest the presence of Co–S bonds<sup>[23]</sup> in the cluster structure (Figure IV.18 left). In the case of S K-edge XANES, the reference samples indicate that the white line intensity decrease and the edge position energy increase with increasing sulfur oxidation, changing from 2471 eV for  $\text{S}^{-2}$  to 2483 eV for  $\text{S}^{6+}$ . From the peak positions in S K-edge XANES of  $\text{Co}_x(\text{SR})_m$  clusters three kinds of sulfur states can be distinguished: a first one at 2471 eV, corresponding to an approximated oxidation state of -1, a second one at 2479 eV to 2481 eV related to oxidized ( $\text{SO}_x$ ) sulfur species, and a third one at 2474 eV corresponding to the S–C bond of the thiolate ligand. The Co–S bond was already observed by Raman and FTIR (Figure IV.15 and Figure IV.16) and is confirmed by Co and S K-edge XANES.

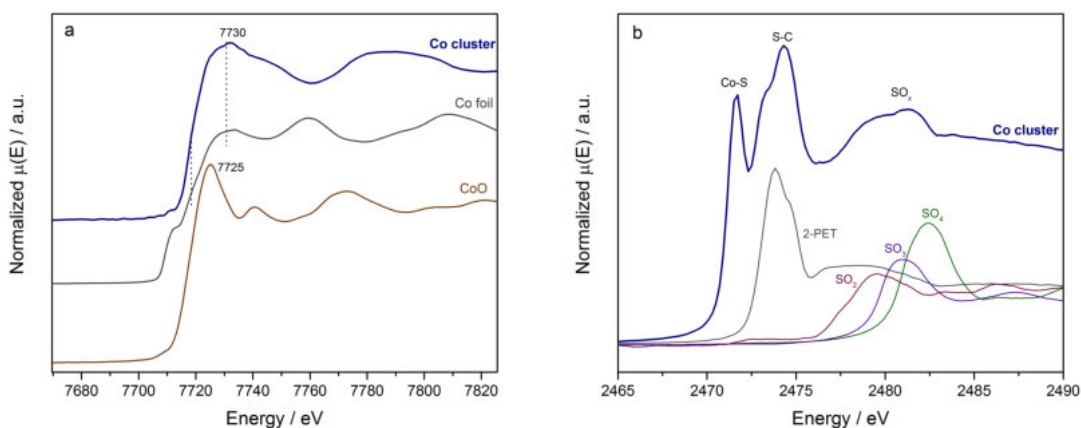


Figure IV.18: (a) XANES spectra at the Co K-edge and (b) S K-edge of the  $\text{Co}_x(\text{SR})_m$  clusters and reference materials.

### IV-3 Conclusions $\text{Co}_x(\text{SR})_m$

Thiolate protected cobalt nanoclusters were synthesized for the first time. Due to cluster fragmentation, their exact molecular mass and/or distribution could not be determined by MALDI-MS. However, taking into account the complementary TG analysis, a cluster size in the range of 25–30 cobalt atoms is expected. This is confirmed by STEM and STM images showing uniform clusters of approximately 2 nm size. The MALDI-MS results also revealed a uniform fragment, corresponding to a monomeric staple unit ( $-\text{S}-\text{Co}-\text{S}-$ ), which was corroborated by Raman. Furthermore, XPS, XAFS and EELS analysis indicated a metallic state of cobalt. The different characterization results point to characteristic structural features and properties of thiolate protected Co clusters. The cobalt clusters were stable in solution, but upon air contact of the dry powder they oxidized and decomposed to a black powder that was insoluble in almost any solvent. XPS analysis together with XANES and FTIR revealed the presence of oxidized sulfur (with two different kinds of sulfur species), which protects the metallic oxidation state of cobalt. Based on the current synthesis and the characterization results, more detailed studies of the exact Co cluster size, composition and physical/chemical properties are to be performed in the near future.

# Chapter V

## $\text{Co}_x\text{Au}_{25-x}(\text{SR})_y$ cluster

### V-1 $\text{Co}_x\text{Au}_{25-x}(\text{SR})_y$ S1

Based on experience (see Chapter IV and from previous work with pure Au clusters) a synthesis approach was tested that focused on the prevention of Co oxidation. Since short reaction times are beneficial for Co clusters (prevents oxidation) and longer reaction times for the formation of Au clusters the experiments were carried out under nitrogen atmosphere in toluene instead of THF. Dreier and Ackerson successfully proved radicals as a requirement for the reaction mechanism of cluster formation by introducing AIBN as radicalstarter in a Au cluster synthesis in toluene<sup>[93]</sup>. In contrast to most radical starters which are based on peroxides AIBN decomposes into  $\text{N}_2$  and two radicals<sup>[94]</sup> and is therefore suitable for this synthesis approach. At 80 °C it has a half life time of 100 min<sup>[95]</sup>. A relatively high amount of Co precursor was used to enhance the chances of incorporation of unoxidized Co into a stable Au nanocluster structure.

### 1 Characterisation of $\text{Co}_x\text{Au}_{25-x}(\text{SR})_y$ S1

The synthesized  $\text{Co}_x\text{Au}_{25-x}(\text{SR})_y$  solution was cleaned and separated by SEC based on previous experience<sup>[55]</sup>. From the SEC separation a total of 12 fractions was isolated. Figure V.1 shows the absorption spectra of the collected samples/fractions measured in THF solvent, except samples 9 and 12 for which the concentration was below the detection limit. Two different tendencies are clearly observed; whereas samples 10 and 11 show pronounced peaks at 402 and 483 nm, the rest of the samples have a unique pronounced band shifting from 517 to 500 nm. The spectra observed for the samples 10 and 11 are similar to the monometallic  $\text{Co}_x(\text{SR})_m$  clusters, with peaks shifted from 416 to 402 nm and from 505 to 483 nm. The UV/Vis spectrum of monometallic  $\text{Au}_{25}(\text{SR})_{18}$  cluster have characteristic peaks at 446, 500, 552 and 680 nm as shown in Figure V.2. Then, the peak at 483 nm could be related with

the doping of the Cobalt into a structure similar to  $\text{Au}_{25}$ , due to the small band that is also observed at 686 nm in sample 11. The samples from 1 to 8 with the peak around 500 nm can be related with larger structures or different numbers of dopant atoms inside the structure, although further separation by HPLC would be required.

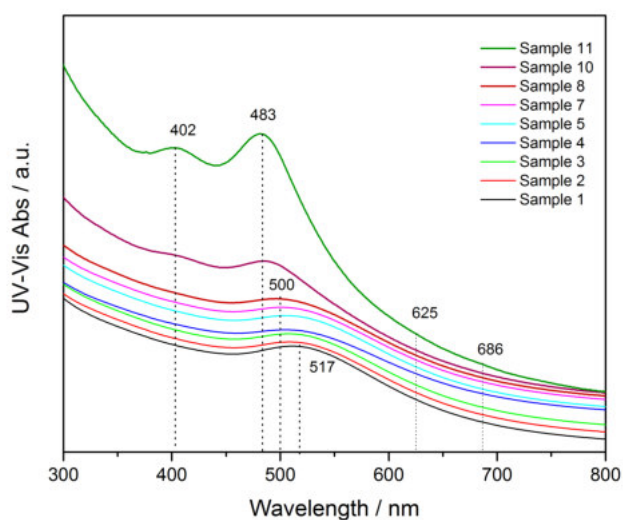


Figure V.1: UV/Vis spectra of fractions from SEC of synthesis S1

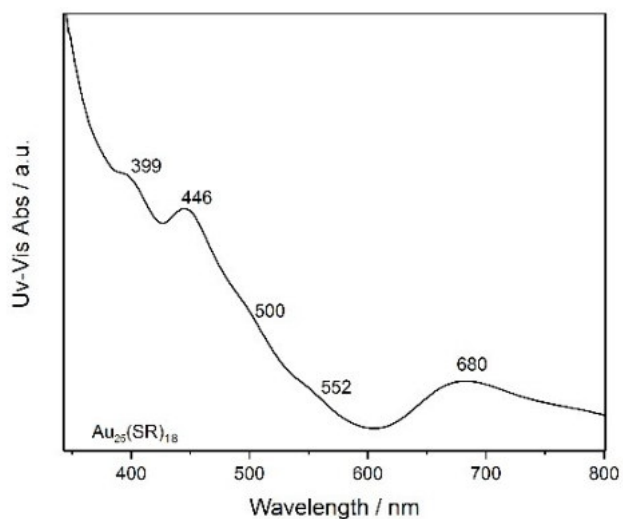


Figure V.2: UV/Vis spectrum of  $\text{Au}_{25}(\text{SR})_{18}$

In order to complement the optical activity studies and elucidate the sizes after the SEC separation, MALDI mass spectroscopy was performed (Figure V.3). The

UV/Vis spectra were measured in THF and then dried for storage. After this step, some of the samples were not dissolving anymore. Not all samples could be further investigated. This may be due to instability of the clusters in atmospheric conditions coming from oxidations.

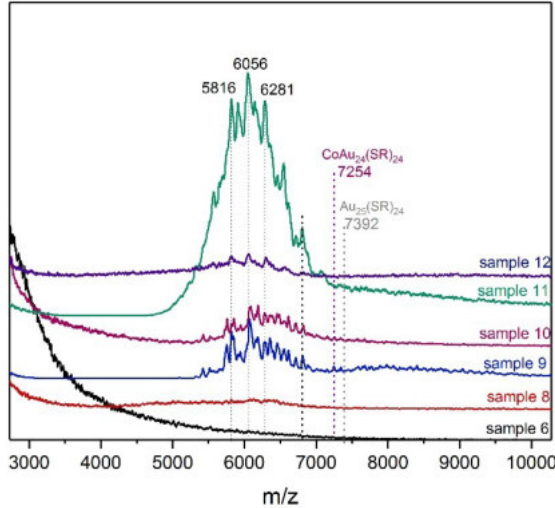


Figure V.3: MALDI spectra of the fractions 6, 8, 9, 10, 11 and 12.

MALDI spectra are shown in detail for the region where the Co doped  $\text{Au}_{25}(\text{SR})_{18}$  clusters (Figure V.3) are expected. A weak peak at 7254 m/z is obtained corresponding to  $\text{CoAu}_{24}(\text{SR})_{18}$  that would be expected in the case of a  $\text{Au}_{25}$  base structure. In the case of Pd or Pt previous work has shown the possibility of introducing only one atom in this structure<sup>[37]</sup>, whereas several number of dopants can be introduced with Cu or Ag<sup>[35,96]</sup>. For single Pt or Pd doping the dopant will take the center core location of the structure, but in the case of Cu the surface of the core is preferred and in the case of Ag positions in the staples are also occupied. Figure V.3 shows a broad distribution of signal around 6056 m/z that could be related to doped Au clusters with different number of Co atoms. Further characterization by ESI or optimization of the matrix should be performed to clarify this point. In comparison to the other fractions, the MALDI and the UV/Vis spectra of sample 11 are in both cases more pronounced. This could be related to higher purity of this sample from the separation.

## V-2 $\text{Co}_x\text{Au}_{25-x}(\text{SR})_y$ S2

In a second approach to obtain cobalt doped gold clusters, a synthesis procedure similar as for Pd or Pt doping of  $\text{Au}_{25}$  clusters was followed<sup>[37]</sup>. In this case a lower

Co/Au ratio than that in the previous synthesis (section V-1) was employed. In this protocol, quaternary amines (TOAB) were used as phase transfer catalysts in THF. Quaternary amines have the tendency to oxidize cobalt. The same applies to peroxides which are formed by THF. A higher gold abundance could enclose cobalt and its oxidation may be partially avoided, but with the downside of decreasing yield.

## 1 Characterization of $\text{Co}_x\text{Au}_{25-x}(\text{SR})_y$ S2

In this case, once the cluster solution was obtained, it was cleaned by methanol to remove excess of thiolate ligand precursor and side products. Following the cleaning, different solvent extractions were performed before further separation steps by SEC were taken. Based on previous work on doped clusters, changes in atomic composition lead to different solubilities<sup>[97]</sup>. In the case of Pd in Au clusters, extraction of the doped structures can be achieved by acetonitrile from the cluster synthesis mixture<sup>[97]</sup>. Acetone can dissolve  $\text{Au}_{25}(\text{SR})_{18}$  but not  $\text{Au}_{38}(\text{SR})_{24}$  or  $\text{Au}_{40}(\text{SR})_{24}$ <sup>[98,55]</sup>, whereas all the clusters are soluble in DCM.

First acetonitrile extraction was performed, followed by acetone and finally the rest was dissolved in DCM. Each batch was separated by SEC independently. Figure V.4 shows the UV/Vis spectra of the purest fraction from each separation batch. The sample from the acetone extraction showed the most defined peaks at 362, 435, 508 and 628 nm, similar to the spectra from the previous synthesis. For the DCM and acetonitrile fractions no defined peaks were observed in the spectra.

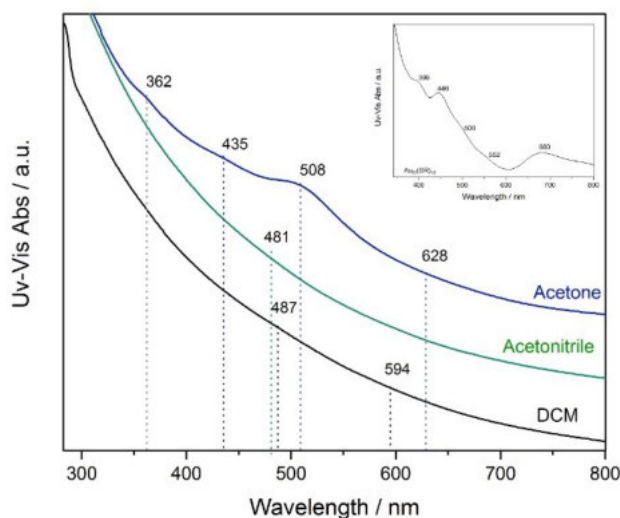


Figure V.4: UV/Vis spectra after SEC of the purest fraction from solvent extraction.



The selected samples were analyzed by MALDI to obtain information about size and composition of the clusters. Figure V.5 shows that all samples contain the desired  $\text{CoAu}_{24}(\text{SR})_{18}$  cluster with the highest presence in the DCM sample. The acetonitrile and acetone samples have a pronounced peak at 6064 m/z that could be related to a  $\text{Co}_2\text{Au}_{19}(\text{SR})_{18}$  cluster.

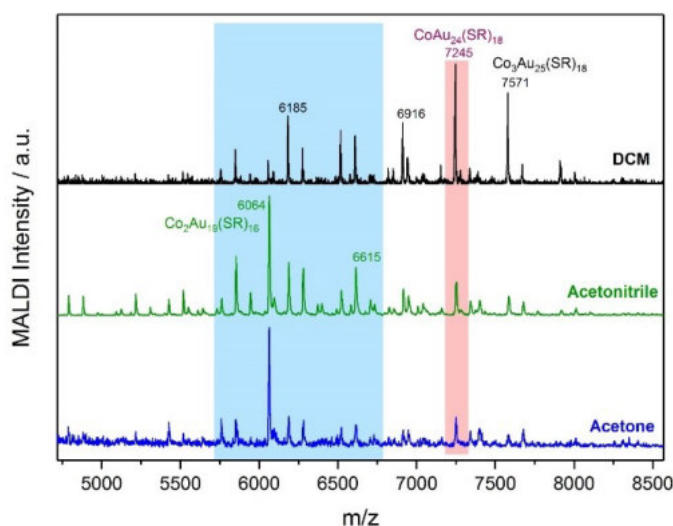


Figure V.5: MALDI spectra of acetonitril, acetone and DCM fraction.

XPS measurements were not able to prove the existence of Co in any of the fractions. This might be due to a relatively low concentration of Co in relation to Au and the C from the ligands. It was also not possible to detect sulfur. To improve the measurement it might help to remove the ligands by thermal treatment to eliminate interfering signal from carbon. Shivhare et al. showed that the cluster size and structure is hardly affected by mild thermal treatment for ligand removal<sup>[99]</sup>.

Preliminary XAFS measurements were performed on solid samples in order to get complementary information about the doped clusters. On the left side of Figure V.6 the S K-edge XANES spectra of the Co doped Au clusters and for reference the  $\text{PdAu}_{24}(\text{SR})_{18}$ , un-doped  $\text{Au}_{25}(\text{SR})_{18}$  and the thiol ligand are shown. A similar tendency to  $\text{Au}_{25}(\text{SR})_{18}$  is observed in all the samples with clear S-C bonds at around 2475 eV related with the ligands and S-Au around 2473 eV. However, the S-Co bond around 2472 eV is clearly detected in the three Co doped Au cluster samples. This could be related to staple or surface core positions of Co atoms inside the cluster structure. On the right side in Figure V.6 the preliminary EXAFS analysis at Au L<sub>3</sub>-edge is shown. The Au-Au bond distances correlate with the  $\text{Au}_{25}$  structure, and a peak close to 2.5 Å is observed like in the case of Pd doped Au cluster which could be related with the incorporation of the heteroatom doping

inside the structure. However, additional measurements at lower temperature and further fitting analysis is required in order to confirm the possible positions of the Co dopant atoms.

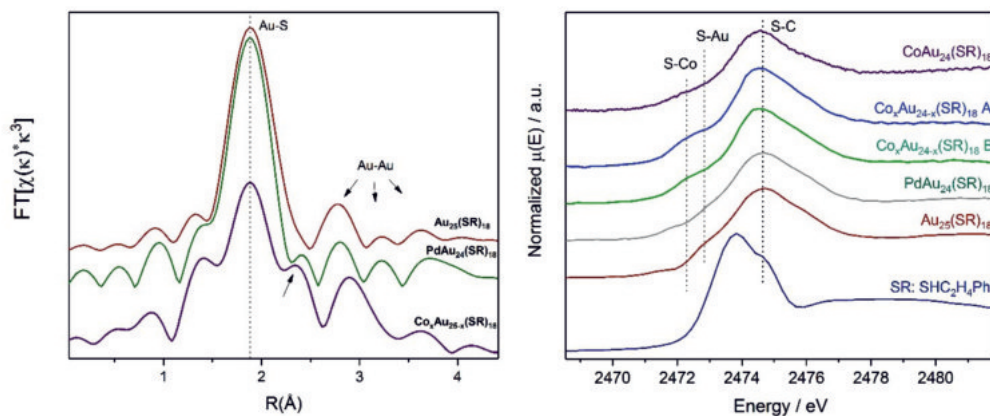


Figure V.6: XAFS of doped gold clusters and references: Left: S K-edge, XANES Right: Au L<sub>3</sub>-edge, R-space

## 2 Theoretical calculations on $\text{Co}_x\text{Au}_{25-x}(\text{SR})_y$ clusters S2

The dopant atom location is crucial information for bimetallic clusters to fully understand their reaction behavior. For this a correlation of experimental data with theoretical calculations (DFT) is required. In a collaboration with Prof. H. Häkkinen's group of the Nanoscience Center of the University of Jyväskylä (Finland), calculations of the optical activity depending on the Co atom position were performed. The results of core center position (A), core surface position (B) and staple position (C) are shown in Figure V.7 (for the calculations only one Co atom was considered). There is a strong influence on the UV/Vis spectra depending on the location of the Co doping atom. In the comparison with the experimental data, position B fits best with the UV/Vis spectra obtained with the acetone extraction sample which is shown in Figure V.8. Accordingly, the expected position of the Co dopant atom would be on the surface of the Au core. This assumption fits with the XAFS measurements where a clear Co-S bond was detected. However, further calculations for more Co dopant atoms and possible combinations of occupations are required.

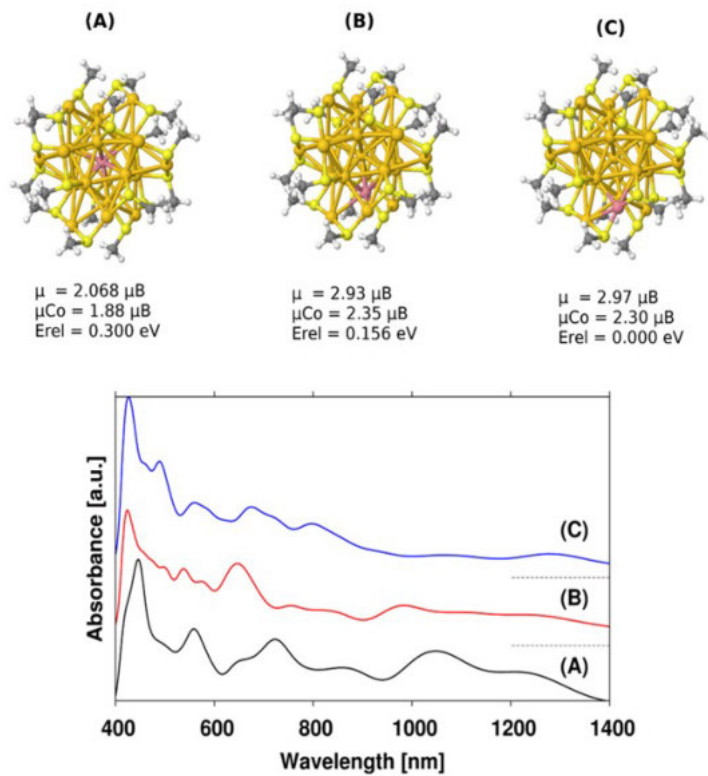


Figure V.7: Calculated UV/Vis spectra of  $\text{CoAu}_{24}(\text{SR})_{18}$  nanoclusters with different dopant positions

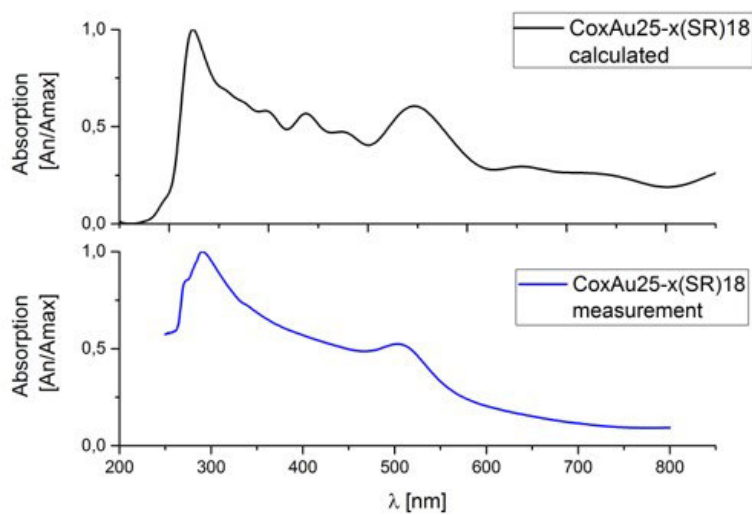


Figure V.8: Comparison of experimental and calculated data

### V-3 Conclusions of $\text{Co}_x\text{Au}_{25-x}(\text{SR})_y$

Preliminary results indicate the successful synthesis of  $\text{CoAu}_{24}(\text{SR})_{18}$  nanoclusters in two different ways. Synthesis approach S1 led to rather large structures that may contain multiple dopant atoms that were partially not stable in air. UV/Vis spectroscopy in combination with MALDI indicated one fraction to contain the desired  $\text{CoAu}_{24}(\text{SR})_{18}$  clusters. For this structure, with Synthesis S2 a similar UV/Vis spectrum and a more pronounced MALDI peak were obtained. The clusters were found in all three solvent extraction fractions from S2 with highest presence in DCM. In the acetonitrile phase MALDI indicated the existence of a  $\text{Co}_2\text{Au}_{19}(\text{SR})_{18}$  cluster. XPS could not confirm the presence of Co in any of the samples, whereas XAFS S K-edge pointed to a similar behavior of the alleged  $\text{CoAu}_{24}(\text{SR})_{18}$  and  $\text{Au}_{25}(\text{SR})_{18}$ . S-C bonds from the ligands as well as S-Co bonds were found. The S-Co bond suggests Co to be either on the cluster core surface or to be in the staple motifs. Based on theoretical calculations the core surface position is more likely. Au  $L_3$ -edge measurements gave the same Au-Au distances as for the  $\text{Au}_{25}(\text{SR})_{18}$  reference, indicating a similar structure.

# Chapter VI

## Catalytic Properties

The catalytic behavior and stability of metal oxide supported cobalt, gold and cobalt doped gold nanoclusters, which are described in previous chapters, were investigated using carbon monoxide oxidation as model reaction. Preliminary in-situ spectroscopic measurements by DRIFTS and XAFS have been done to correlate the catalytic activity to the cluster properties. The monometallic cobalt clusters did not show catalytic activity in the reaction. A strong influence of the Co dopant on the catalytic behavior compared to the pure gold cluster could be observed, however, this chapter presents preliminary results. Further investigations are required and will be performed in the near future.

### VI-1 Catalyst characterization

Elemental analysis was performed by GIXRF. The spectra of Co/Au-CeO<sub>2</sub> and Au-CeO<sub>2</sub> catalysts are shown in Figure VI.1 and Figure VI.2, respectively. The results of the elemental analysis calculated by fundamental parameters are shown in Table VI.1. In theory, for 22 atoms of gold a single cobalt atom is present, which is in agreement with expectations, since the fractions from SEC contained CoAu<sub>24</sub>(SR)<sub>18</sub> and Au<sub>25</sub>(SR)<sub>18</sub>, which could not be fully separated from the doped clusters. The Au<sub>25</sub> catalyst has a lower loading compared to the cobalt doped Au catalysts.

Table VI.1: Weight and atomic ratio of Ce, Au and Co from Au/Co–CeO<sub>2</sub> and Au<sub>25</sub>–CeO<sub>2</sub> catalysts.

Element	Line	Weight [%]	Atom [%]
Au/Co–CeO <sub>2</sub>			
Co	Ka	0.007	0.0174
Ce	La	99.465	99.607
Au	La	0.527	0.375
Au <sub>25</sub> –CeO <sub>2</sub>			
Ce	La	99.670	99.765
Au	La	0.330	0.235

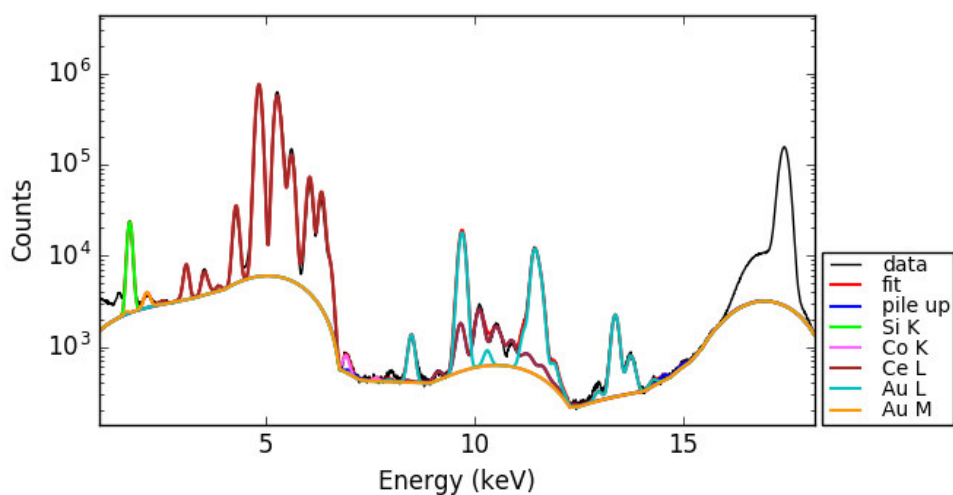


Figure VI.1: GIXRF spectrum and fitting of the Au/Co–CeO<sub>2</sub> catalyst

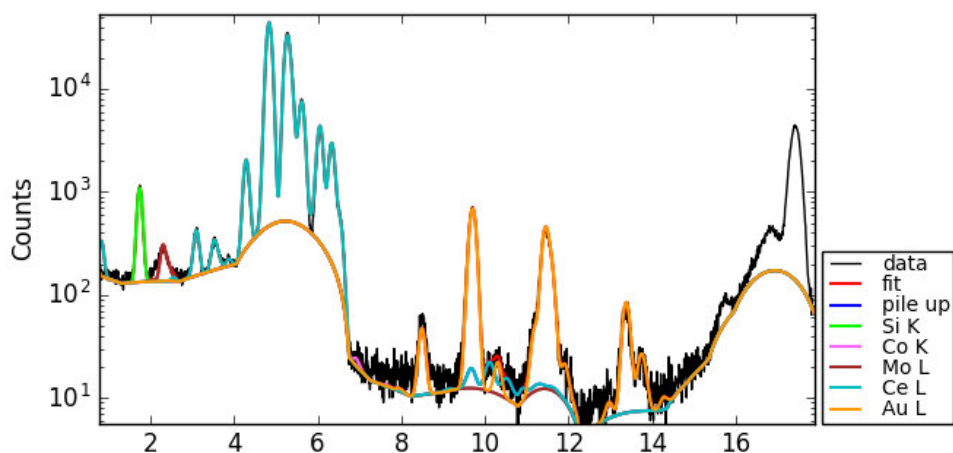


Figure VI.2: GIXRF spectrum and fitting of the Au<sub>25</sub>–CeO<sub>2</sub> catalyst

## VI-2 Catalytic activity in CO oxidation

The CO oxidation reaction was carried out inside the in-situ cell described in the experimental Chapter III-7, which was also used for DRIFTS and XAFS measurements during the reaction. The outlet of the cell was directly connected to a MS that allowed to follow the catalytic behaviour. Temperature programmed reaction (TPR) measurements were done in the temperature range from 40 °C to 200 °C or 300 °C, depending on the sample, with a heating rate of 5 °C/min. All samples were pretreated in-situ at 150 °C in 5% O<sub>2</sub> in Ar for 30 min. Figure VI.3 and Figure VI.5 show the MS signal of H<sub>2</sub>O, CO, CO<sub>2</sub> and O<sub>2</sub> normalized to Ar, plotted in logarithmic form versus the reaction temperature. On the left side the evolution of the reactants and products during the heating process is shown, while on the right side the affected cooling can be discerned. Figures VI.4 and VI.6 highlight the hysteresis in CO conversion from the two catalysts.

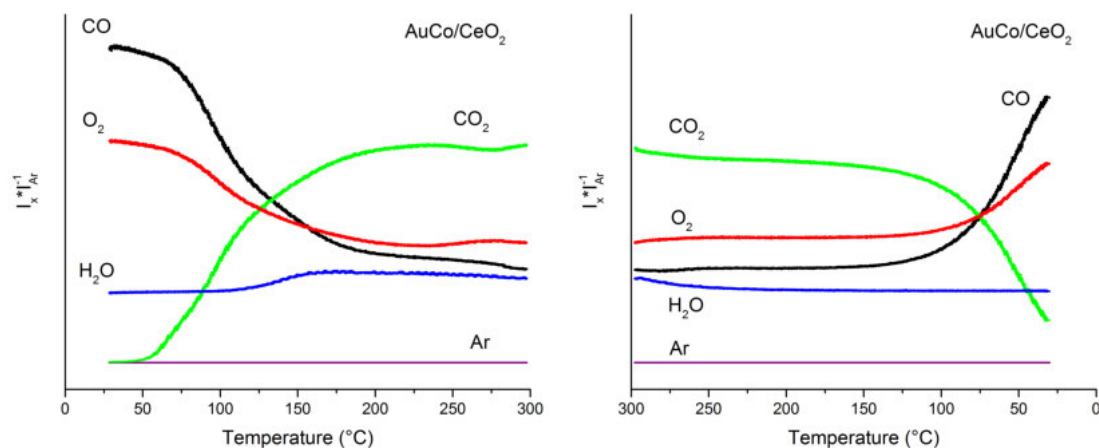


Figure VI.3: MS spectra of CO, CO<sub>2</sub>, H<sub>2</sub>O and O<sub>2</sub> during CO-oxidation on Au/Co-CeO<sub>2</sub> catalyst.

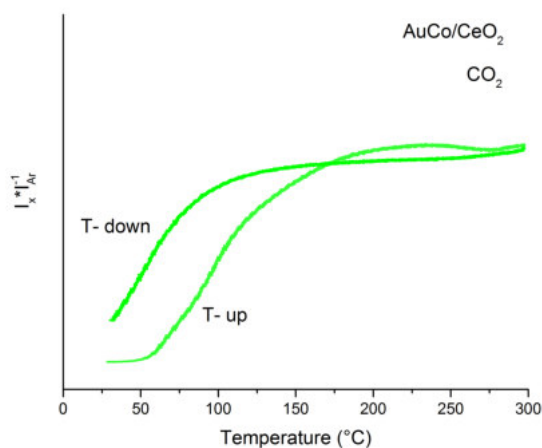


Figure VI.4: Hysteresis of CO conversion on Au/Co-CeO<sub>2</sub> catalyst.

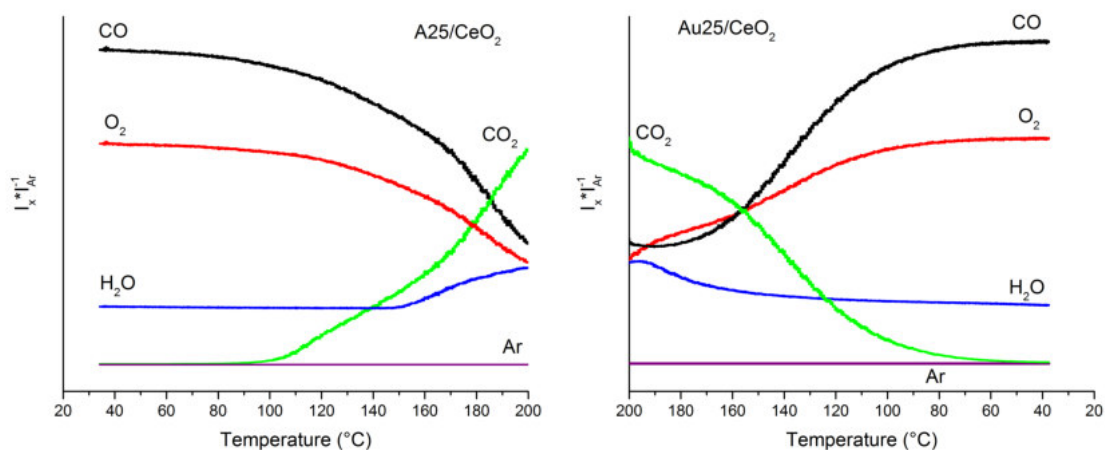


Figure VI.5: MS spectra of CO, CO<sub>2</sub>, H<sub>2</sub>O and O<sub>2</sub> during CO-oxidation experiment on Au<sub>25</sub>-CeO<sub>2</sub> catalyst.

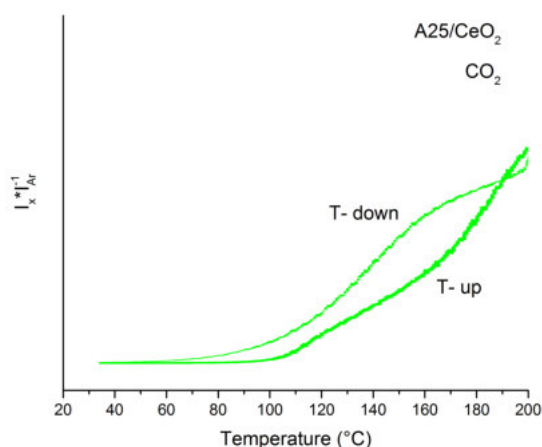


Figure VI.6: Hysteresis of CO conversion on Au<sub>25</sub>-CeO<sub>2</sub> catalyst.

CO<sub>2</sub> formation starts around 50 °C in the case of the Co doped Au clusters, rising with temperature till a stable state around 200 °C is revealed. CO and O<sub>2</sub> consumption follows the increase of CO<sub>2</sub> formation till around 150 °C when it slows down to a stable state. This stable state is maintained during the cooling process till around 75 °C where decrease in conversion is observed. In the case of un-doped Au<sub>25</sub> catalyst higher temperature around 100 °C is required for CO<sub>2</sub> formation, which increases with temperature but with smaller slope in comparison to the doped system. After reaching the maximum temperature of 200 °C and start of the cooling process the activity drops immediately. In both cases water formation is detected, although the catalysts were pre-treated in O<sub>2</sub>/Ar at 150 °C.

In order to compare the activity of the Au/Co-CeO<sub>2</sub> and the Au<sub>25</sub>-CeO<sub>2</sub> catalyst, the real amount of active sites in each sample must be carefully taken into account. Figure VI.7 shows the intensity of the MS signal of CO<sub>2</sub> normalized by the intensity



of Ar and divided by the total mass of the catalyst and the atomic ratio of support to active sites (Au, Co). The normalization with Argon cancels possible artifacts coming from variations of the gas. CO<sub>2</sub> was used for the analysis since CO has the same mass as N<sub>2</sub> and minimal air leaks cannot be ruled out.

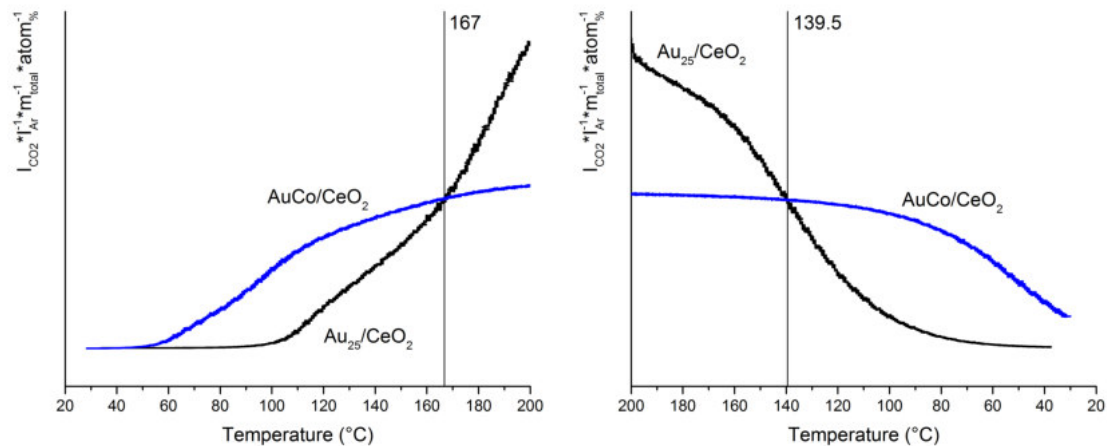


Figure VI.7: Comparison of the CO oxidation activity: normalized CO<sub>2</sub> MS signal of Au/Co–CeO<sub>2</sub> and Au<sub>25</sub>–CeO<sub>2</sub> catalyst.

Once normalized, the same tendencies are obtained: CO conversion starts about 50 °C lower for the Co doped catalyst than for the pure Au; a pronounced activity rise till 120 °C reaching a stable state with the doped cluster catalysts. The decrease in the reaction onset temperature can be associated with the cobalt dopants, since the pure Co clusters from Chapter IV on ceria did not show any activity for CO oxidation. Then, the changes observed in the catalytic activity should be related to changes in the electronic configuration and properties of the gold clusters induced by the cobalt dopant.

### VI–3 In situ DRIFT studies

In situ DRIFT measurements taken during the reaction on the CoAu/CeO<sub>2</sub> catalysts are shown in Figure VI.8. The spectra are plotted in intervals of 50 °C, during heating and as well as cooling. Previous studies from Wu et al. reported DRIFT bands of CO adsorption on different Au and Ce sites of pretreated thiolate protected Au<sub>25</sub>(SR)<sub>18</sub> clusters supported on CeO<sub>2</sub><sup>[44]</sup>. The same bands could be observed during the experiment, but with slight shifts due to temperature effects and different number of adsorbed CO. Less adsorbed CO can be related to less interacting dipoles, that results in a shift to lower wavenumbers, while shifts to higher frequency can be related to an increase in the temperature. The characteristic bands at 2177 cm<sup>-1</sup> related with CO–Ce and the region of CO–Au signals are marked in Figure VI.8

by a brown background. On the right side a purple box highlights a band around  $2145\text{ cm}^{-1}$  which is not observed for pure  $\text{Au}_{25}(\text{SR})_{18}$  clusters and assigned to CO–Co vibrations. This band is only appearing after the reaction, once there is no more activity. This may be related with structural changes or mobility of the Co atoms inside the cluster structure, that make cobalt atoms accessible to interact with CO.

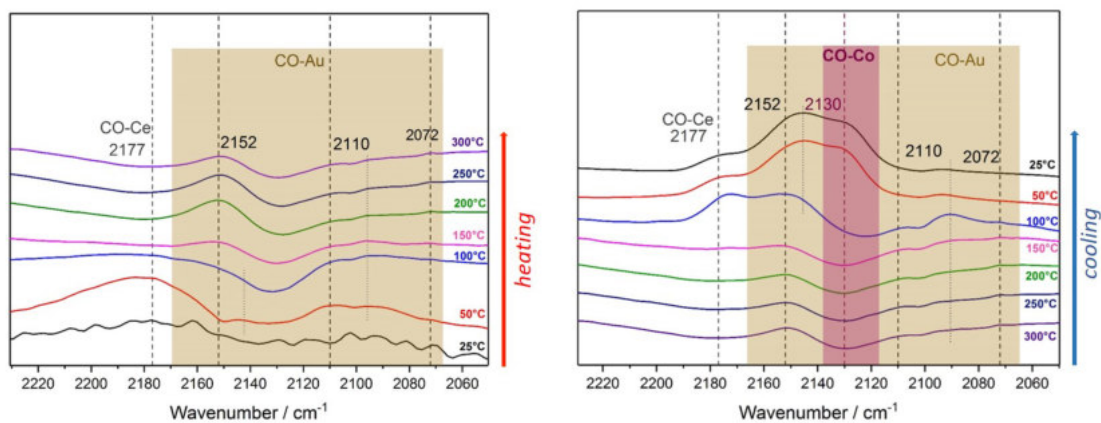


Figure VI.8: DRIFT spectra of CoAu catalyst under reaction conditions at different temperatures.

## VI-4 XAFS

Figure VI.9 shows the XANES region of the Au/Co–ceria catalyst measured of the Au  $L_3$ -edge. The Au  $L_3$ -edge XANES probe 2p electrons to unoccupied 5d states of all the Au atoms in the clusters, therefore the Au–S bonding in these structures is observed. The white line intensity increases from bulk to cluster structure, indicating the d–electron depletion as the size decreases. From calculations, it is also observed that staple Au sites which are non–metallic show a more pronounced d–electron depletion than the metallic core Au sites.

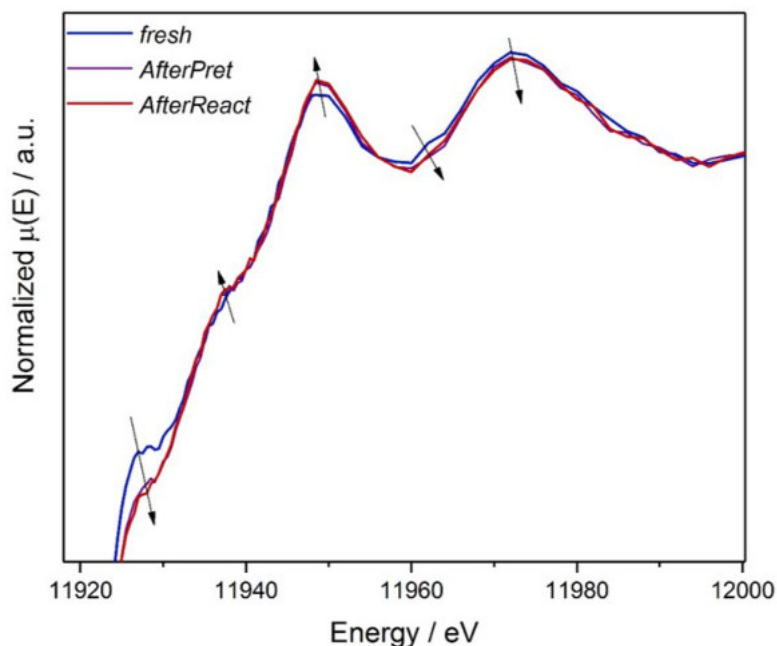


Figure VI.9: XAFS  $L_3$ : XANES region of Au/Co catalyst on  $CeO_2$ : fresh, after pretreatment and after reaction

There is a decrease of the whiteline and a small shift to higher binding energies between the fresh sample and the pretreated one. The change in the whiteline is due to the broken staple bonds (Au-S) due to pretreatment. Once the catalyst is pretreated, its enhanced stability under reactive conditions is indicated by the almost unchanged spectrum. For Fourier transformation in EXAFS, oscillation up to 10 K were taken into account and plotted in R-space, which is shown in Figure VI.10. Because of the relative low amount of clusters compared to the support material, the quality of data did not allow EXAFS fitting. Figure VI.10 shows only qualitative data since a shift up to  $0.5 \text{ \AA}$  has to be expected because of the phase problem of the detector. Upon pretreatment and reaction the relative contribution to the signal of Au-Au increases, this is again resulting from the broken staple bonds.

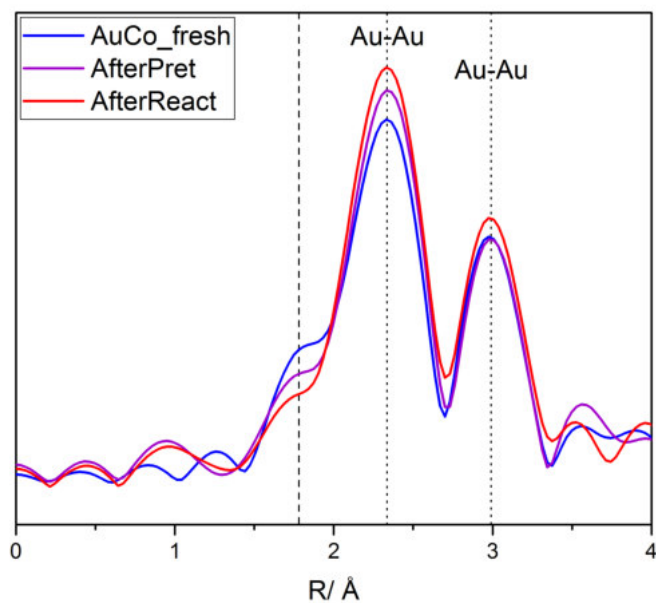


Figure VI.10: XAFS Au L<sub>3</sub>: R-space of Au/Co on CeO<sub>2</sub> catalyst: fresh, after pretreatment and after reaction.

## VI-5 Conclusions of Catalytic Properties

Supported Co<sub>x</sub>(SR)<sub>m</sub> clusters did not show any catalytic activity in CO oxidation. In contrast, cobalt doped gold clusters were active and clearly showed a different behavior than the Au<sub>25</sub>(SR)<sub>18</sub> reference. The presence of incorporated Co atoms reduced the reaction on-set temperature by 50 °C, compared to Au<sub>25</sub>(SR)<sub>18</sub>. During the reaction water formation was observed for pure and doped Au catalysts, despite the O<sub>2</sub>/Ar pretreatment at 150 °C. DRIFTS measurements revealed an additional band that can be associated with Co-CO interactions during cooling at the end of the reaction. XAFS measurements clearly showed the breaking of staple bonds due to the pretreatment. The spectra before and after reaction hardly differed indicating a stable structure.

# Chapter VII

## Discussion

Thiolate protected cobalt nanoclusters in the size range of 2 nm with 25 to 30 atoms were synthesized for the first time. Monomeric staple fragments were revealed by MALDI and substantiated by Raman, in addition to XPS, XAFS and EELS analysis which pointed to cobalt in metallic state, indicating a successful synthesis of monometallic cobalt clusters. The clusters show longtime stability in solution but when exposed to air they decompose. Two different kinds of oxidized sulfur species were revealed by XPS analysis together with XANES and FTIR.

XAFS, MALDI and UV/Vis spectroscopy point to a successful synthesis of doped  $\text{CoAu}_{24}(\text{SR})_{18}$  clusters by two different approaches. Synthesis S1 additionally led to large structures with low stability in air. Longer reaction times could break those down to smaller stable structures. Synthesis S2 had a higher yield of the desired product. MALDI also indicated the presence of a  $\text{Co}_2\text{Au}_{19}(\text{SR})_{18}$  cluster only to be found in the acetonitrile phase. XAFS showed similar characteristics for the  $\text{CoAu}_{24}(\text{SR})_{18}$  sample and the  $\text{Au}_{25}(\text{SR})_{18}$  reference, which emphasizes the synthesis success.

$\text{Co}_x(\text{SR})_m$  clusters supported on  $\text{CeO}_2$  were not catalytic active in CO oxidation, whereas CO oxidation with the  $\text{Au}_{25}(\text{SR})_{18}\text{-CeO}_2$  catalyst started around 100 °C. However, the onset temperature for the CO conversion could be drastically decreased by 50 °C by incorporating Co dopant atoms into the gold clusters. After a reaction cycle with a maximum temperature of 300 °C a new band in the DRIFTS spectrum of the cobalt doped Au catalyst appeared that could be related to Co–CO vibrations; further investigations are needed to verify this hypothesis. The ligand removal of the clusters by  $\text{O}_2/\text{Ar}$  pretreatment was observed by XAFS. XANES spectra proved the stability of the clusters during reaction.

To complete this research topic, further experiments have to be performed. Structural information about the new clusters is key to get deeper insight. This could be achieved by investigations with EXAFS at lower temperature ( $\text{He}(l)$ ) or crystallization could give definite proof of the cluster structure. To continue, syn-

thesis methods have to be improved in order to obtain higher yields. Separation could be increased by HPLC, in addition to SEC, to obtain truly monodisperse doped clusters for further investigations and rational catalyst design.

# Chapter VIII

## Appendix

### 1 Supporting information

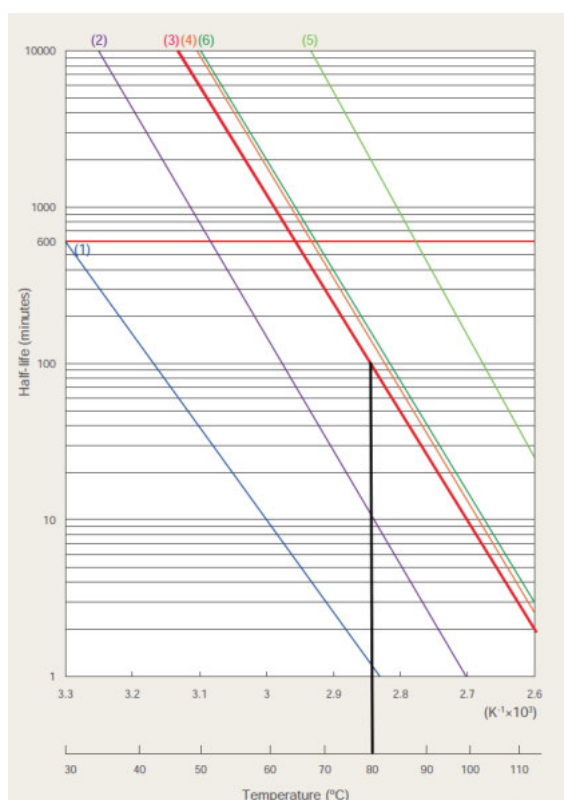


Figure VIII.1: Temperature dependency of the half life time of AIBN (red). The graphic was reproduced from Wako<sup>[95]</sup>.

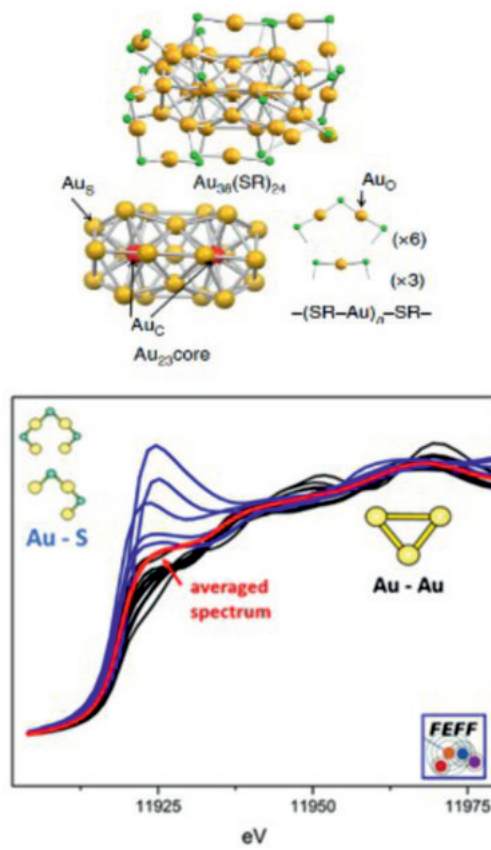


Figure VIII.2: Calculations of XANES spectra of  $\text{Au}_{38}(\text{SR})_{24}$   $L_3$ -edge with FEFF9<sup>[100]</sup>.



## 2 References

### Article references

- [2] Rongchao Jin et al. „Atomically Precise Colloidal Metal Nanoclusters and Nanoparticles: Fundamentals and Opportunities“. In: *Chemical Reviews* 116.18 (2016), pp. 10346–10413. DOI: 10.1021/acs.chemrev.5b00703.
- [3] Yizhong Lu and Wei Chen. „Sub-nanometre sized metal clusters: from synthetic challenges to the unique property discoveries“. In: *Chemical Society Reviews* 41.9 (2012), p. 3594. DOI: 10.1039/c2cs15325d.
- [4] Rongchao Jin. „Atomically precise metal nanoclusters: stable sizes and optical properties“. In: *Nanoscale* 7.5 (2015), pp. 1549–1565. DOI: 10.1039/c4nr05794e.
- [5] Zhikun Wu et al. „Well-Defined Nanoclusters as Fluorescent Nanosensors: A Case Study on Au<sub>25</sub>(SG)<sub>18</sub>“. In: *Small* 8.13 (2012), pp. 2028–2035. DOI: 10.1002/smll.201102590.
- [6] Junya Yoshimoto et al. „Optical Properties of 2-Methacryloyloxyethyl Phosphorylcholine-Protected Au<sub>4</sub>Nanoclusters and Their Fluorescence Sensing of C-Reactive Protein“. In: *The Journal of Physical Chemistry C* 119.25 (2015), pp. 14319–14325. DOI: 10.1021/acs.jpcc.5b03934.
- [7] Zhentao Luo, Kaiyuan Zheng, and Jianping Xie. „Engineering ultrasmall water-soluble gold and silver nanoclusters for biomedical applications“. In: *Chem. Commun.* 50.40 (2014), pp. 5143–5155. DOI: 10.1039/c3cc47512c.
- [8] Yan Zhu, Huifeng Qian, and Rongchao Jin. „Catalysis opportunities of atomically precise gold nanoclusters“. In: *Journal of Materials Chemistry* 21.19 (21 2011), p. 6793. DOI: 10.1039/c1jm10082c.
- [9] Seiji Yamazoe, Kiichirou Koyasu, and Tatsuya Tsukuda. „Nonscalable Oxidation Catalysis of Gold Clusters“. In: *Acc. Chem. Res.* 47.3 (47 2014), pp. 816–824. DOI: 10.1021/ar400209a.
- [10] Yuichi Negishi et al. „A Critical Size for Emergence of Nonbulk Electronic and Geometric Structures in Dodecanethiolate-Protected Au Clusters“. In: *Journal of the American Chemical Society* 137.3 (2015), pp. 1206–1212. DOI: 10.1021/ja5109968.
- [11] Seiji Yamazoe, Kiichirou Koyasu, and Tatsuya Tsukuda. „Nonscalable Oxidation Catalysis of Gold Clusters“. In: *Accounts of Chemical Research* 47.3 (2013), pp. 816–824. DOI: 10.1021/ar400209a.

- [12] Takeshi Iwasa and Katsuyuki Nobusada. „Theoretical Investigation of Optimized Structures of Thiolated Gold Cluster [Au<sub>25</sub>(SCH<sub>3</sub>)<sub>18</sub>]“. In: *The Journal of Physical Chemistry C* 111.1 (2007), pp. 45–49. DOI: 10.1021/jp063532w.
- [13] Manzhou Zhu et al. „Correlating the Crystal Structure of A Thiol-Protected Au<sub>25</sub>Cluster and Optical Properties“. In: *Journal of the American Chemical Society* 130.18 (2008), pp. 5883–5885. DOI: 10.1021/ja801173r.
- [15] Jianwei Ji et al. „Thiolate-protected Ni<sub>39</sub>and Ni<sub>41</sub>nanoclusters: synthesis, self-assembly and magnetic properties“. In: *Nanoscale* 6.15 (6 2014), p. 9185. DOI: 10.1039/c4nr01063a.
- [16] Husain N. Kagalwala et al. „Photocatalytic Hydrogen Generation System Using a Nickel-Thiolate Hexameric Cluster“. In: *Inorganic Chemistry* 52.15 (52 2013), pp. 9094–9101. DOI: 10.1021/ic4013069.
- [17] Min Zhu et al. „Reduction-resistant and reduction-catalytic double-crown nickel nanoclusters“. In: *Nanoscale* 6.23 (6 2014), pp. 14195–14199. DOI: 10.1039/c4nr04981k.
- [18] Anindya Ganguly et al. „A copper cluster protected with phenylethanethiol“. In: *Journal of Nanoparticle Research* 15.4 (2013), p. 1522. DOI: 10.1007/s11051-013-1522-8.
- [19] Shridevi Bhat et al. „Atomically precise and monolayer protected iridium clusters in solution“. In: *RSC Advances* 6.32 (6 2016), pp. 26679–26688. DOI: 10.1039/c5ra27972k.
- [20] Puentes V. F., Krishnan K. M., and Alivisatos A. P. „Colloidal Nanocrystal Shape and Size Control: The Case of Cobalt.“ In: *Science* (291 2001), pp. 2115–2117. DOI: 10.1126/science.1058495.
- [21] G. Carotenuto et al. „Preparation and characterization of cobalt-based nanostructured materials“. In: *The European Physical Journal B* 31.4 (31 2003), pp. 545–551. DOI: 10.1140/epjb/e2003-00064-0.
- [22] Nusrat J. M. Sanghamitra and Shyamalava Mazumdar. „Effect of Polar Solvents on the Optical Properties of Water-Dispersible Thiol-Capped Cobalt Nanoparticles“. In: *Langmuir* 24.7 (24 2008), pp. 3439–3445. DOI: 10.1021/la702876h.
- [23] Nikolay Kornienko et al. „Operando Spectroscopic Analysis of an Amorphous Cobalt Sulfide Hydrogen Evolution Electrocatalyst“. In: *Journal of the American Chemical Society* 137.23 (137 2015), pp. 7448–7455. DOI: 10.1021/jacs.5b03545.

- [24] Wenxin Zhu et al. „Nickel sulfide microsphere film on Ni foam as an efficient bifunctional electrocatalyst for overall water splitting“. In: *Chemical Communications* 52.7 (52 2016), pp. 1486–1489. DOI: 10.1039/c5cc08064a.
- [25] Chih-Jung Chen et al. „An integrated cobalt disulfide (CoS<sub>2</sub>) co-catalyst passivation layer on silicon microwires for photoelectrochemical hydrogen evolution“. In: *Journal of Materials Chemistry A* 3.46 (2015), pp. 23466–23476. DOI: 10.1039/c5ta06202k.
- [26] Xiyu Zhao et al. „NiCo-selenide as a novel catalyst for water oxidation“. In: *Journal of Materials Science* 51.8 (51 2016), pp. 3724–3734. DOI: 10.1007/s10853-015-9690-9.
- [27] Zijun Sun et al. „Core-shell amorphous cobalt phosphide/cadmium sulfide semiconductor nanorods for exceptional photocatalytic hydrogen production under visible light“. In: *Journal of Materials Chemistry A* 4.5 (2016), pp. 1598–1602. DOI: 10.1039/c5ta07561k.
- [28] Zhen-Feng Huang et al. „Hollow Cobalt-Based Bimetallic Sulfide Polyhedra for Efficient All-pH-Value Electrochemical and Photocatalytic Hydrogen Evolution“. In: *Journal of the American Chemical Society* 138.4 (2016), pp. 1359–1365. DOI: 10.1021/jacs.5b11986.
- [29] Viacheslav Iablokov et al. „Catalytic CO Oxidation over Well-Defined Cobalt Oxide Nanoparticles: Size-Reactivity Correlation“. In: *ACS Catalysis* 5.10 (5 2015), pp. 5714–5718. DOI: 10.1021/acscatal.5b01452.
- [30] Chuanhao Yao et al. „Mono-cadmium vs Mono-mercury Doping of Au<sub>25</sub> Nanoclusters“. In: *Journal of the American Chemical Society* 137.49 (2015), pp. 15350–15353. DOI: 10.1021/jacs.5b09627.
- [31] Stephen L. Christensen et al. „Dopant Location, Local Structure, and Electronic Properties of Au<sub>24</sub>Pt(SR)<sub>18</sub> Nanoclusters“. In: *The Journal of Physical Chemistry C* 116.51 (2012), pp. 26932–26937. DOI: 10.1021/jp310183x.
- [32] Yuichi Negishi et al. „Formation of a Pd@Au<sub>12</sub> Superatomic Core in Au<sub>24</sub>Pd<sub>1</sub>(SC<sub>12</sub>H<sub>25</sub>)<sub>18</sub> Probed by <sup>197</sup>Au Mössbauer and Pd K-Edge EXAFS Spectroscopy“. In: *The Journal of Physical Chemistry Letters* 4.21 (2013), pp. 3579–3583. DOI: 10.1021/jz402030n.
- [33] Mathias Brust et al. „Synthesis of thiol-derivatised gold nanoparticles in a two-phase Liquid-Liquid system“. In: *J. Chem. Soc., Chem. Commun.* 7 (1994), pp. 801–802. DOI: 10.1039/c39940000801.
- [34] Christina A. Fields-Zinna et al. „Mass Spectrometry of Small Bimetal Monolayer-Protected Clusters“. In: *Langmuir* 25.13 (2009), pp. 7704–7710. DOI: 10.1021/la803865v.

- [35] Yuichi Negishi et al. „Effect of Copper Doping on Electronic Structure, Geometric Structure, and Stability of Thiolate-Protected Au<sub>25</sub> Nanoclusters“. In: *The Journal of Physical Chemistry Letters* 3.16 (2012), pp. 2209–2214. DOI: 10.1021/jz300892w.
- [36] Noelia Barrabés, Bei Zhang, and Thomas Bürgi. „Racemization of Chiral Pd<sub>2</sub>Au<sub>36</sub>(SC<sub>2</sub>H<sub>4</sub>Ph)<sub>24</sub>: Doping Increases the Flexibility of the Cluster Surface“. In: *Journal of the American Chemical Society* 136.41 (2014), pp. 14361–14364. DOI: 10.1021/ja507189v.
- [37] Annelies Sels et al. „Structural Investigation of the Ligand Exchange Reaction with Rigid Dithiol on Doped (Pt, Pd) Au<sub>25</sub> Clusters“. In: *The Journal of Physical Chemistry C* 121.20 (2017), pp. 10919–10926. DOI: 10.1021/acs.jpcc.6b12066.
- [39] Huifeng Qian et al. „Monoplatinum Doping of Gold Nanoclusters and Catalytic Application“. In: *Journal of the American Chemical Society* 134.39 (2012), pp. 16159–16162. DOI: 10.1021/ja307657a.
- [40] Masatake Haruta et al. „Novel Gold Catalysts for the Oxidation of Carbon Monoxide at a Temperature far Below 0 °C“. In: *Chemistry Letters* 16.2 (1987), pp. 405–408. DOI: 10.1246/c1.1987.405.
- [41] G AVGOUROPOULOS et al. „Catalytic performance and characterization of Au/doped-ceria catalysts for the preferential CO oxidation reaction“. In: *Journal of Catalysis* 256.2 (2008), pp. 237–247. DOI: 10.1016/j.jcat.2008.03.014.
- [42] Jacob Good et al. „On the functional role of the cerium oxide support in the Au<sub>38</sub>(SR)<sub>24</sub>/CeO<sub>2</sub> catalyst for CO oxidation“. In: *Catalysis Today* 280 (2017), pp. 239–245. DOI: 10.1016/j.cattod.2016.04.016.
- [43] Xiaotao Nie et al. „CeO<sub>2</sub>-supported Au<sub>38</sub>(SR)<sub>24</sub> nanocluster catalysts for CO oxidation: a comparison of ligand-on and -off catalysts“. In: *Nanoscale* 5.13 (2013), p. 5912. DOI: 10.1039/c3nr00970j.
- [44] Zili Wu et al. „Thiolate Ligands as a Double-Edged Sword for CO Oxidation on CeO<sub>2</sub> Supported Au<sub>25</sub>(SCH<sub>2</sub>CH<sub>2</sub>Ph)<sub>18</sub> Nanoclusters“. In: *Journal of the American Chemical Society* 136.16 (2014), pp. 6111–6122. DOI: 10.1021/ja5018706.
- [45] Olga Lopez-Acevedo et al. „Quantum size effects in ambient CO oxidation catalysed by ligand-protected gold clusters“. In: *Nature Chemistry* 2.4 (2010), pp. 329–334. DOI: 10.1038/nchem.589.

- [46] Weili Li et al. „Catalytic CO Oxidation Using Bimetallic  $MxAu_{25-x}$  Clusters: A Combined Experimental and Computational Study on Doping Effects“. In: *The Journal of Physical Chemistry C* 120.19 (2016), pp. 10261–10267. DOI: 10.1021/acs.jpcc.6b00793.
- [47] Arvind Varma et al. „Solution Combustion Synthesis of Nanoscale Materials“. In: *Chemical Reviews* 116.23 (2016), pp. 14493–14586. DOI: 10.1021/acs.chemrev.6b00279.
- [48] N. Barrabés et al. „Study of Pt–CeO<sub>2</sub> interaction and the effect in the selective hydrodechlorination of trichloroethylene“. In: *Applied Catalysis B: Environmental* 87.1-2 (2009), pp. 84–91. DOI: 10.1016/j.apcatb.2008.08.018.
- [49] Niklas Nilius et al. „Model Catalysts Based on Au Clusters and Nanoparticles“. In: (2013), pp. 91–138. DOI: 10.1007/430\_2013\_135.
- [50] D. Ingerle et al. „A new spectrometer for grazing incidence X-ray fluorescence for the characterization of Arsenic implants and Hf based high k layers“. In: *Spectrochimica Acta Part B: Atomic Spectroscopy* 65.6 (2010), pp. 429–433. DOI: 10.1016/j.sab.2010.02.015.
- [51] B. Ravel and M. Newville. „ATHENA,ARTEMIS,HEPHAESTUS: data analysis for X-ray absorption spectroscopy usingIFEFFIT“. In: *Journal of Synchrotron Radiation* 12.4 (12 2005), pp. 537–541. DOI: 10.1107/s0909049505012719.
- [52] Gian Luca Chiarello et al. „Adding diffuse reflectance infrared Fourier transform spectroscopy capability to extended x-ray-absorption fine structure in a new cell to study solid catalysts in combination with a modulation approach“. In: *Review of Scientific Instruments* 85.7 (2014), p. 074102. DOI: 10.1063/1.4890668.
- [53] Stephan Pollitt et al. „Synthesis and Properties of Monolayer-Protected Cox(SC<sub>2</sub>H<sub>4</sub>Ph)<sub>m</sub> Nanoclusters“. In: *The Journal of Physical Chemistry C* 121.20 (2017), pp. 10948–10956. DOI: 10.1021/acs.jpcc.6b12076.
- [54] R.J. Kern. „Tetrahydrofuran complexes of transition metal chlorides“. In: *Journal of Inorganic and Nuclear Chemistry* 24.9 (1962), pp. 1105–1109. DOI: 10.1016/0022-1902(62)80255-3.
- [55] Stefan Knoppe et al. „Size Exclusion Chromatography for Semipreparative Scale Separation of Au<sub>38</sub>(SR)<sub>24</sub> and Au<sub>40</sub>(SR)<sub>24</sub> and Larger Clusters“. In: *Analytical Chemistry* 83.13 (2011), pp. 5056–5061. DOI: 10.1021/ac200789v.
- [56] Risako Tsunoyama et al. „MALDI Mass Analysis of 11 kDa Gold Clusters Protected by Octadecanethiolate Ligands†“. In: *The Journal of Physical Chemistry C* 114.38 (114 2010), pp. 16004–16009. DOI: 10.1021/jp101741a.

- [57] Joseph B. Tracy et al. „Electrospray Ionization Mass Spectrometry of Uniform and Mixed Monolayer Nanoparticles: Au<sub>25</sub>[S(CH<sub>2</sub>)<sub>2</sub>Ph]<sub>18</sub> and Au<sub>25</sub>[S(CH<sub>2</sub>)<sub>2</sub>Ph]<sub>18-x</sub>(SR)<sub>x</sub>“. In: *Journal of the American Chemical Society* 129.51 (2007), pp. 16209–16215. DOI: 10.1021/ja076621a.
- [58] Christina A. Fields-Zinna et al. „Mass Spectrometry of Small Bimetal Monolayer-Protected Clusters“. In: *Langmuir* 25.13 (2009), pp. 7704–7710. DOI: 10.1021/la803865v.
- [59] Amala Dass et al. „FAB Mass Spectrometry of Au<sub>25</sub>(SR)<sub>18</sub> Nanoparticles“. In: *Analytical Chemistry* 80.18 (2008), pp. 6845–6849. DOI: 10.1021/ac801259j.
- [60] Kellen M. Harkness et al. „Surface Fragmentation of Complexes from Thiolate Protected Gold Nanoparticles by Ion Mobility-Mass Spectrometry“. In: *Analytical Chemistry* 82.7 (2010), pp. 3061–3066. DOI: 10.1021/ac100251d.
- [61] Kellen M. Harkness, David E. Cliffler, and John A. McLean. „Characterization of thiolate-protected gold nanoparticles by mass spectrometry“. In: *The Analyst* 135.5 (2010), p. 868. DOI: 10.1039/b922291j.
- [62] Laurence A. Angel et al. „Ion Mobility Mass Spectrometry of Au<sub>25</sub>(SCH<sub>2</sub>CH<sub>2</sub>Ph)<sub>18</sub> Nanoclusters“. In: *ACS Nano* 4.8 (2010), pp. 4691–4700. DOI: 10.1021/nn1012447.
- [63] Wen Liu et al. „A highly active and stable hydrogen evolution catalyst based on pyrite-structured cobalt phosphosulfide“. In: *Nature Communications* 7 (2016), p. 10771. DOI: 10.1038/ncomms10771.
- [64] Pandian Ganesan et al. „Cobalt Sulfide Nanoparticles Grown on Nitrogen and Sulfur Codoped Graphene Oxide: An Efficient Electrocatalyst for Oxygen Reduction and Evolution Reactions“. In: *ACS Catalysis* 5.6 (2015), pp. 3625–3637. DOI: 10.1021/acscatal.5b00154.
- [65] Oleg Yeshchenko et al. „Optical properties of sol-gel fabricated Co/SiO<sub>2</sub> nanocomposites“. In: *Physica E: Low-dimensional Systems and Nanostructures* 41.1 (41 2008), pp. 60–65. DOI: 10.1016/j.physe.2008.06.003.
- [66] Jin Zhang and Christopher Q. Lan. „Nickel and cobalt nanoparticles produced by laser ablation of solids in organic solution“. In: *Materials Letters* 62.10-11 (2008), pp. 1521–1524. DOI: 10.1016/j.matlet.2007.09.038.
- [67] R A Ganeev. „Nonlinear refraction and nonlinear absorption of various media“. In: *Journal of Optics A: Pure and Applied Optics* 7.12 (2005), pp. 717–733. DOI: 10.1088/1464-4258/7/12/004.

- [68] Wentao Wei et al. „One-Pot Synthesis, Photoluminescence, and Electrocatalytic Properties of Subnanometer-Sized Copper Clusters“. In: *Journal of the American Chemical Society* 133.7 (2011), pp. 2060–2063. DOI: 10.1021/ja109303z.
- [69] Stephan Link et al. „Visible to Infrared Luminescence from a 28-Atom Gold Cluster“. In: *The Journal of Physical Chemistry B* 106.13 (2002), pp. 3410–3415. DOI: 10.1021/jp014259v.
- [70] Vivian Wing-Wah Yam, Eddie Chung-Chin Cheng, and Zhong-Yuan Zhou. „A Highly Soluble Luminescent Decanuclear Gold(I) Complex with a Propeller-Shaped Structure“. In: *Angewandte Chemie International Edition* 39.9 (2000), pp. 1683–1685. DOI: 10.1002/(sici)1521-3773(20000502)39:9<1683::aid-anie1683>3.0.co;2-1.
- [71] T. P. Bigioni, R. L. Whetten, and Ö. Dag. „Near-Infrared Luminescence from Small Gold Nanocrystals“. In: *The Journal of Physical Chemistry B* 104.30 (2000), pp. 6983–6986. DOI: 10.1021/jp993867w.
- [72] Philip Ewels et al. „A Complete Overhaul of the Electron Energy-Loss Spectroscopy and X-Ray Absorption Spectroscopy Database: Eelsdb.Eu.“ In: *Microscopy and Microanalysis* 22.03 (2016), pp. 717–724. DOI: 10.1017/s1431927616000179.
- [73] Yuan Zhao et al. „In situ electron energy loss spectroscopy study of metallic Co and Co oxides“. In: *Journal of Applied Physics* 108.6 (2010), p. 063704. DOI: 10.1063/1.3482013.
- [74] A. Taylor and R. W. Floyd. „Precision measurements of lattice parameters of non-cubic crystals“. In: *Acta Crystallographica* 3.4 (1950), pp. 285–289. DOI: 10.1107/s0365110x50000732.
- [75] S G Lyapin et al. „Raman studies of nearly half-metallic ferromagnetic CoS<sub>2</sub>“. In: *Journal of Physics: Condensed Matter* 26.39 (2014), p. 396001. DOI: 10.1088/0953-8984/26/39/396001.
- [76] Zulipiya Shadike et al. „Improved electrochemical performance of CoS<sub>2</sub>-MWCNT nanocomposites for sodium-ion batteries“. In: *Chemical Communications* 51.52 (2015), pp. 10486–10489. DOI: 10.1039/c5cc02564h.
- [77] E. Anastassakis and C. H. Perry. „Light scattering and ir measurements in XS<sub>2</sub> pyrite-type compounds“. In: *The Journal of Chemical Physics* 64.9 (1976), pp. 3604–3609. DOI: 10.1063/1.432711.

- [78] Birte Varnholt et al. „Structural Information on the Au–S Interface of Thiolate-Protected Gold Clusters: A Raman Spectroscopy Study“. In: *The Journal of Physical Chemistry C* 118.18 (2014), pp. 9604–9611. DOI: 10.1021/jp502453q.
- [79] Thomas Bürgi. „Properties of the gold–sulphur interface: from self-assembled monolayers to clusters“. In: *Nanoscale* 7.38 (2015), pp. 15553–15567. DOI: 10.1039/c5nr03497c.
- [80] Yurui Xue et al. „Quantifying thiol–gold interactions towards the efficient strength control“. In: *Nature Communications* 5 (2014), p. 4348. DOI: 10.1038/ncomms5348.
- [81] Birte Varnholt et al. „Vibrational Coupling Modulation in n-Alkanethiolate Protected Au<sub>25</sub>(SR)<sub>180</sub> Clusters“. In: *The Journal of Physical Chemistry C* 120.44 (2016), pp. 25378–25386. DOI: 10.1021/acs.jpcc.6b07592.
- [82] Alfredo Tlahuice-Flores. „Ligand Effects on the Structure and Vibrational Properties of the Thiolated Au<sub>18</sub> Cluster.“ In: *Progress in Natural Science: Materials International* 26.5 (2016), pp. 510–515. DOI: 10.1016/j.pnsc.2016.09.008.
- [83] Birte Varnholt et al. „Structural Information on the Au–S Interface of Thiolate-Protected Gold Clusters: A Raman Spectroscopy Study“. In: *The Journal of Physical Chemistry C* 118.18 (2014), pp. 9604–9611. DOI: 10.1021/jp502453q.
- [84] Alfredo Tlahuice-Flores, Robert L. Whetten, and Miguel Jose-Yacamán. „Vibrational Normal Modes of Small Thiolate-Protected Gold Clusters“. In: *The Journal of Physical Chemistry C* 117.23 (2013), pp. 12191–12198. DOI: 10.1021/jp4033063.
- [85] Joseph F. Parker et al. „Electron Self-exchange Dynamics of the Nanoparticle Couple [Au<sub>25</sub>(SC<sub>2</sub>Ph)<sub>18</sub>]0/1-By Nuclear Magnetic Resonance Line-Broadening“. In: *The Journal of Physical Chemistry C* 112.36 (2008), pp. 13976–13981. DOI: 10.1021/jp805638x.
- [86] Liliana Lukashuk et al. „Operando XAS and NAP-XPS studies of preferential CO oxidation on Co<sub>3</sub>O<sub>4</sub> and CeO<sub>2</sub>-Co<sub>3</sub>O<sub>4</sub> catalysts“. In: *Journal of Catalysis* 344 (2016), pp. 1–15. DOI: 10.1016/j.jcat.2016.09.002.
- [87] Peng Zhang. „X-ray Spectroscopy of Gold–Thiolate Nanoclusters“. In: *The Journal of Physical Chemistry C* 118.44 (2014), pp. 25291–25299. DOI: 10.1021/jp507739u.



- [88] P. Ferstl et al. „Adsorption and Activation of CO on Co<sub>3</sub>O<sub>4</sub>(111) Thin Films“. In: *The Journal of Physical Chemistry C* 119.29 (2015), pp. 16688–16699. DOI: 10.1021/acs.jpcc.5b04145.
- [89] Feng Tao et al. „Electrochemical characterization on cobalt sulfide for electrochemical supercapacitors“. In: *Electrochemistry Communications* 9.6 (2007), pp. 1282–1287. DOI: 10.1016/j.elecom.2006.11.022.
- [90] Sébastien Devillers et al. „1-Dodecanethiol Self-Assembled Monolayers on Cobalt“. In: *Langmuir* 27.24 (2011), pp. 14849–14860. DOI: 10.1021/la2026957.
- [91] Sujitra Pookpanratana et al. „Self-Assembled Monolayers Impact Cobalt Interfacial Structure in Nanoelectronic Junctions“. In: *The Journal of Physical Chemistry C* 119.12 (2015), pp. 6687–6695. DOI: 10.1021/acs.jpcc.5b00816.
- [92] B. J. Lindberg et al. „Molecular Spectroscopy by Means of Esca Ii. Sulfur Compounds. Correlation of Electron Binding Energy with Structure.“ In: *Phys. Scr.* (1 1970), p. 286.
- [93] Timothy A. Dreier and Christopher J. Ackerson. „Radicals Are Required for Thiol Etching of Gold Particles“. In: *Angewandte Chemie International Edition* 54.32 (2015), pp. 9249–9252. DOI: 10.1002/anie.201502934.
- [96] Xinyue Dou et al. „Facile synthesis of water-soluble Au<sub>25</sub>-xAg<sub>x</sub> nanoclusters protected by mono- and bi-thiolate ligands“. In: *Chemical Communications* 50.56 (2014), p. 7459. DOI: 10.1039/c4cc02261k.
- [98] Huifeng Qian and Rongchao Jin. „Ambient Synthesis of Au<sub>144</sub>(SR)<sub>60</sub>Nanoclusters in Methanol“. In: *Chemistry of Materials* 23.8 (2011), pp. 2209–2217. DOI: 10.1021/cm200143s.
- [99] Atal Shivhare et al. „Following the Thermal Activation of Au<sub>25</sub>(SR)<sub>18</sub> Clusters for Catalysis by X-ray Absorption Spectroscopy“. In: *The Journal of Physical Chemistry C* 117.39 (2013), pp. 20007–20016. DOI: 10.1021/jp4063687.
- [100] John J. Rehr et al. „Parameter-free calculations of X-ray spectra with FEFF9“. In: *Physical Chemistry Chemical Physics* 12.21 (2010), p. 5503. DOI: 10.1039/b926434e.

## Book references

- [1] T. Tsukuda and H. Häkkinen. *Protected Metal Clusters: From Fundamentals to Applications*. Elsevier Health Sciences, Sept. 1, 2015. 372 pp. ISBN:

9780081000861. URL: [http://www.ebook.de/de/product/24243159/protected\\_metal\\_clusters\\_from\\_fundamentals\\_to\\_applications.html](http://www.ebook.de/de/product/24243159/protected_metal_clusters_from_fundamentals_to_applications.html).

- [38] Bei ZHANG. *Thiolate protected gold nanoclusters: heteroatom doping and catalysis*. Univ. Geneve, 2016. DOI: 10.13097/archive-ouverte/unige:91470. URL: <https://archive-ouverte.unige.ch/unige:91470>.
- [94] JEAN-PIERRE SCHIRMANN and PAUL BOURDAUDUCQ. *Hydrazine. Ullmann's encyclopedia of industrial chemistry*. Ed. by Weinheim Wiley-VCH Verlag GmbH & Co. KGaA. 2012. DOI: 10.1002\14356007.a13\_177.
- [97] Annelies Sels. *LIGAND EXCHANGE REACTIONS WITH PALLADIUM, PLATINUM DOPED Au<sub>25</sub>(SR)<sub>18</sub> CLUSTERS*. Universite De Geneve, 2015.

## Web references

- [14] Alexander Kulesza. *Thiolate-protected gold cluster*. Ed. by Wikipedia. 2017. URL: <https://commons.wikimedia.org/w/index.php?curid=20479091>.
- [95] Wako Pure Chemical Industries Ltd. *Azo Polymerization Initiator Comprehensive Catalog 25*. Ed. by Wako Pure Chemical Industries Ltd. 2016. URL: [https://www.wako-chemicals.de/files/download/pdf/wako\\_azo\\_polymerization\\_initiators\\_catalog\\_25.pdf](https://www.wako-chemicals.de/files/download/pdf/wako_azo_polymerization_initiators_catalog_25.pdf).